

Cosmology before noon with multiple galaxy populations

Haruki Ebina ^{a,b,c} and Martin White ^{a,b,c}

^aDepartment of Physics, University of California, Berkeley, CA 94720, USA

^bBerkeley Center for Cosmological Physics, UC Berkeley, CA 94720, USA

^cLawrence Berkeley National Laboratory, One Cyclotron Road, Berkeley, CA 94720, USA

E-mail: ebina@berkeley.edu, mwhite@berkeley.edu

Abstract. Near-future facilities observing the high-redshift universe ($2 < z < 5$) will have an opportunity to take advantage of “multi-tracer” cosmology by observing multiple tracers of the matter density field: Lyman alpha emitters (LAE), Lyman break galaxies (LBG), and CMB lensing κ . In this work we use Fisher forecasts to investigate the effect of multi-tracers on next-generation facilities. In agreement with previous work, we show that multiple tracers improve constraints primarily from degeneracy breaking, instead of the traditional intuition of sample variance cancellation. Then, we forecast that for both BBN and CMB primary priors, the addition of lensing and LAEs onto a LBG-only sample will gain 25% or more in many parameters, with the largest gains being factor of ~ 10 improvement for f_{EDE} . We include a preliminary approach towards modelling the impact of radiative transfer (RT) on forecasts involving LAEs by introducing a simplified model at linear theory level. Our results, albeit preliminary, show that while RT influences LAE-only forecasts strongly, its effect on composite multi-tracer forecasts is limited.

Contents

1	Introduction	1
2	Tracers of large-scale structure at high redshift	2
2.1	Lyman Alpha Emitters	3
2.2	Lyman Break Galaxies	6
2.3	CMB Lensing	8
3	Theory and formalism	9
3.1	Model	9
3.2	Parameters	10
3.3	2D power spectrum	12
3.4	Fisher formalism	13
3.5	Benefits of multi-tracer cosmology	14
4	Multitracer	14
4.1	Linear	15
4.2	Nonlinear	17
5	Radiative transfer	18
6	Results	19
6.1	Growth rate	20
6.2	Standard model	22
6.3	Distances	23
6.4	Neutrino mass and light relics	24
6.5	Primordial features	26
6.6	Early dark energy	27
7	Conclusions	29
A	Variance of measurements with correlation	30
B	Conventions of limiting luminosity in literature	31
C	Counterterms	31

1 Introduction

The large-scale structure of the Universe arises from primordial fluctuations in space-time in the very early Universe, acted upon by gravitational instability in a dark-matter-dominated Universe over many Gyr [1–4]. As such it provides us with a window into fundamental physics and all of the constituents, processes and parameters that influence the evolution of large-scale structure even in subtle ways. In turn this has led to exciting proposals for next-generation facilities that can make high precision measurements of the quasi-linear modes that contain such a wealth of information [5–9].

Much of the focus of these next generation facilities will be measurements of large-scale structure at redshifts above $z \sim 1 - 2$ in order to take advantage of several simultaneous, advantageous trends [10]. First, probing a wide lever arm in time (redshift) is critical to disentangle evolutionary influences from primordial ones and leads to rotated degeneracy directions that tighten joint constraints. Second, the larger volume and smaller scale of non-linearity both allow a larger lever arm in scale to break degeneracies between cosmological and nuisance parameters. Third, the modes are in the linear or quasi-linear regime and carry information from the early Universe before it has been lost to non-linear evolution.

A fundamental limitation to how well we can probe fundamental physics and cosmology comes from the influence of complex astrophysical processes that affect the clustering of objects on the length scales that we observe. This influence is usually described by a set of bias parameters [11] whose form is dictated by the symmetries of our problem (e.g. rotational invariance, the equivalence principle, ...). The ability to break degeneracies between these bias parameters and the fundamental parameters of interest is key to the success of the program. Such degeneracy breaking is dramatically improved if we have multiple tracers of the same underlying density fluctuations with different (or no) biases, such as multiple galaxy populations (known as “multi-tracer”; [12]) or gravitational lensing (of the CMB; [13, 14]). Traditionally, multitracer has been considered in the context of ‘sample variance cancellation’, which avoids the payment of sample variance by measuring quantities, such as ratios of biases, at field level. However, for our forecast we will not have high enough number densities for this to be interesting, nor will we present forecasts for parameters that can be measured at field level.

At $z > 2$ there are two sets of galaxies that make natural targets for spectroscopic surveys: Lyman break galaxies (LBGs) and Lyman alpha emitters (LAEs). LBGs are massive, actively star-forming galaxies with a luminosity approximately proportional to their stellar mass. They are abundant, well studied and well understood [15–17]. By contrast LAEs are compact, metal-poor, star-forming galaxies with $\text{SFR} \sim 1 - 10 M_{\odot}\text{yr}^{-1}$ that live in much lower mass halos and consequently are expected to have significantly lower bias [18]. These two classes of targets naturally possess different biases, making them ideal laboratories for the multi-tracer approach. In addition we have lensing of the CMB, which provides a (projected) tracer of the matter field itself (i.e. with no biases) which further serves to break degeneracies.

In this paper we extend the Fisher formalism developed in ref. [5] to the case of multiple galaxy populations (plus the CMB lensing already included in [5]) and forecast the improvement in constraining power that this provides. The outline of the paper is as follows. In §2, we introduce and characterize the three matter density tracers. In §3 we describe the theoretical framework used for forecasting, including the modelling of biased tracers and the Fisher information formalism. In §4 we then investigate the mechanism of multi-tracer cosmology through forecasting of simplified galaxy tracers with varying characteristics. §5 explains our approach to radiative transfer (RT), which potentially poses concerns toward the use of LAEs as tracers. Finally in §6 we present our forecasts for two experiment designs, Stage 4.5, motivated by DESI II, and Stage V, and conclude in §7 with discussion.

2 Tracers of large-scale structure at high redshift

In this section we describe the relevant properties of the three tracers used for this study; Lyman alpha emitters (LAEs), Lyman break galaxies (LBGs), and gravitational lensing.

For the galaxy tracers we determine the large-scale bias, b , and comoving number density, \bar{n} , of the objects based on previous astronomical surveys that have probed these tracers at the redshifts of relevance. The distinction between these tracers is made primarily by observational technique than physical properties, causing overlap of these populations in many cases.

2.1 Lyman Alpha Emitters

Lyman alpha emitters (LAEs) are young, low-mass, actively star-forming galaxies at high redshift [18, 19]. In the astronomical literature the designation is primarily determined by the method of sample selection, and LAEs are normally selected from narrow or intermediate band imaging surveys as galaxies having large rest-frame equivalent width Ly α emission [18, 20]. While practical, this designation complicates the physical interpretation of the population. Although the dominant physical origins of these emissions (e.g. young massive stars, AGNs, and shock heating with minimal absorption by dust) have been identified [18], a complete understanding of what determines the high Ly α emissivity of LAEs has not yet been obtained. Although we will largely follow the observational designation, from the perspective of cosmology the primary interest will be in the ability to obtain a redshift for the galaxy, which is more closely associated with line flux. There may also be arguments for having detectable continuum emission in order to minimize radiative transfer effects on the galaxy selection.

Due to the method of selection, the characterization of the LAE population for the purpose of cosmological forecasts contains some subtleties and difficulties. The majority of LAE surveys probe faint populations over relatively small areas of sky, whereas the ideal objects for wide-field spectroscopy tend to be brighter and not well-represented in such surveys. Pure narrow-band selection is also not likely to be an efficient means of finding galaxies over large cosmological volumes due to the limited comoving depth each filter provides. For this reason future cosmological surveys will likely rely on targets selected, at least in part, from medium-band imaging. The extent to which the clustering properties of medium band selected objects differ from those selected in narrow bands remains to be quantified. This, along with varying observational definitions of LAE across literature (e.g. whether to include an equivalent width cut, and if so of what value, or whether to include objects with no continuum emission), means our estimates have an element of uncertainty. It is to be expected that differences in sky area coverage, redshift range, and instrumentation between existing surveys and next-generation cosmological facilities indicate that galaxy populations will likely not be identical between them.

The currently ongoing ODIN (One-hundred-deg² DECam Imaging in Narrowbands) survey [21] is amongst the widest of existing LAE surveys (100deg²), though even this is at least a factor of 50 less volume than the samples considered in this work. Unfortunately, the clustering properties of the ODIN sample have not been published, so we primarily rely on previous surveys of even smaller areas, such as the Slicing COSMOS 4K (SC4K) survey [22, 23] at $\sim 2\text{deg}^2$. While the SC4K covers significantly less area than ODIN, it provides a wider range of redshifts through the use of multiple narrow- and medium-band filters. Though the samples are still not an ideal match for the cosmological samples we envision, they represent our current best observational constraints on such populations.

The two key parameters for our forecasts will be the abundance and large-scale clustering of LAEs, as determined by the 3D number density (\bar{n}) and large-scale bias (b). In order to

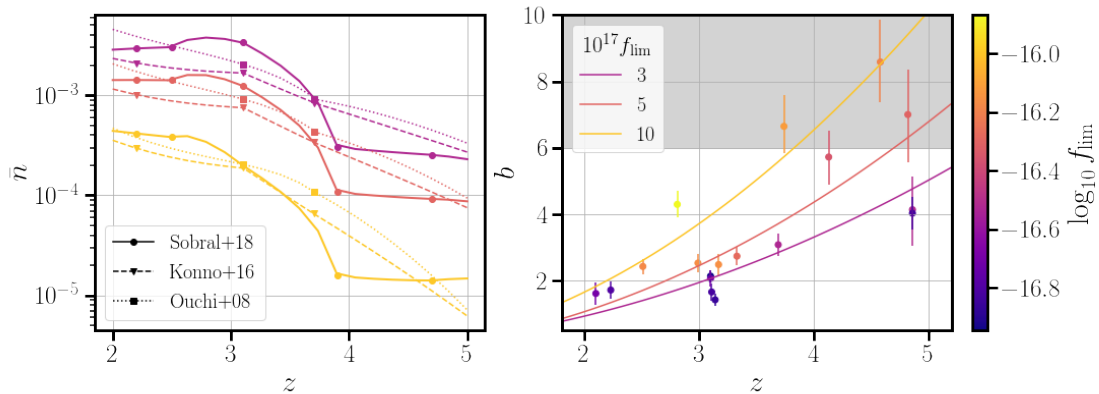


Figure 1: Left: 3D number density (\bar{n}) of LAEs found using Schechter function fits to LF from previous studies [22, 24, 25]. The point markers refer to the values reported in the original studies, while the lines use interpolations of Schechter LF parameters. We see that although there is rough consistency across the literature, a ‘factor of two’ difference is not uncommon. We take the LF parameters from SC4K [22] as our fiducial model in what follows. Right: Large scale bias b of LAEs reported across the literature with various redshift and line flux limits [23, 26–31]. The solid lines show the fit of Eq. (2.4) for $f_{\text{lim}} = 3, 5$ and $10 \times 10^{-17} \text{ erg cm}^{-2} \text{ s}^{-1}$. The region $b \geq 6$ is shaded, as populations with such high bias are not traditionally used for cosmology.

determine these we make use of published studies [22–30], which we discuss further below. The final inputs are shown in Figure 1.

LAE luminosity functions (LF) are frequently quoted in terms of the Ly α luminosity and fit with the Schechter functional form [32]. While the uncertainties in the three parameters of the Schechter function are often covariant, this information is not usually provided which makes assessing uncertainties in \bar{n} more difficult. Thus, we choose to compare different surveys as an estimate of uncertainty. This has the advantage of also including sample variance due to survey volume, though it unfortunately mixes differences in observational selection into the uncertainty.

Assuming a Schechter LF the number density, \bar{n} , of objects brighter than some minimum luminosity, L_{lim} , can be written in terms of three parameters (ϕ^* , L^* and α) as

$$\bar{n}(z) = \ln 10 \int_{\log_{10} L_{\text{lim}}}^{\infty} \phi^* \left(\frac{L}{L^*} \right)^{1+\alpha} e^{-L/L^*} d \log_{10} L \quad (2.1)$$

where L is the Ly α line luminosity. As it ties more directly to observational ‘cost’, we will typically use the line flux (f) instead of luminosity, the two are related by $L = 4\pi f D_L^2(z)$, with D_L the luminosity distance.

In Figure 1, we compare number densities using various LF parameters from different surveys [22, 24, 25]. While there is rough consistency, there are frequently factors of ~ 2 between curves, suggesting our estimates of \bar{n} are likely uncertain ‘at the factor of two level’. We will investigate the impact of this later in §6. We adopt the LF from the SC4K survey [22] as our fiducial model. Since the LF-derived number densities reflect the total number of galaxies at a given line flux limit after correcting for incompleteness, we further include an estimated 50% selection and redshift efficiency.

For our forecasts we will also need to understand the large-scale bias of these populations, which is more complex than the number densities. Existing surveys quote a range of different measures (see e.g. Fig. 3 of ref. [23] for a recent compilation). The clustering strength in LAE surveys is often quoted in terms of a correlation length, r_0 , assuming a power-law (real-space) correlation function:

$$\xi_{gg}(r) = \left(\frac{r}{r_0}\right)^\gamma \quad (2.2)$$

and the power-law index γ is often held fixed (typically to -1.8) in the fit. Given that astronomical LAE surveys typically have discrete narrow- or medium-band selection over a small field, in practice r_0 is obtained by fitting the angular correlation function, $w(\theta)$, to a power-law. Ignoring redshift-space distortions (RSD) the projection of an isotropic 3D correlation, $\xi(r)$, to 2D would give $w(\theta) \propto \theta^\beta$ with $\beta = \gamma + 1$. The presence of redshift-space distortions leads to appreciable changes in this relation on scales comparable to the depth of the shell in comoving distance, an effect that is usually neglected in the literature.

Given the limited information available, we will convert the reported r_0 values to large-scale biases by working to linear order in bias, in which case

$$b^2 = \frac{\xi_{gg}}{\xi_{mm}} \quad (2.3)$$

Again, any RSD contribution to the linear power-spectrum is ignored assuming that the constraints are primarily from scales much smaller than the depth of the survey. A subtlety involved here is that while we are using the linear approximation for the bias, the power-law approximation for ξ_{gg} assumes nonlinear growth which is normally associated with non-linear, scale-dependent bias. Although this poses an inconsistency in our approach, considering higher order biases or re-investigating raw data to find the exact form of ξ_{gg} goes well beyond the scope of this work and likely will not alter the conclusions of this study significantly. It would be worthwhile to refine these estimates when a new analysis of the clustering of LAEs over wide areas becomes available.

This method for estimating the bias requires us to make a number of choices. We evaluate b by computing the ratio in Eq. 2.3 at a fixed scale, r . Since the above estimation assumes that the power-law approximation of ξ_{gg} is valid we choose an angular scale of $\theta \sim 235''$. The validity of the power-law approximation at this scale across surveys and redshifts can be confirmed through inspection of the power-law fit to the angular correlation in the literature [23, 26]. This scale corresponds to $r \simeq 5 h^{-1} \text{Mpc}$ at $z = 3$, and $5 h^{-1} \text{Mpc}$ is large enough to be in the quasi-linear regime for $z > 2$ while being smaller than the typical survey depth to reduce the impact of RSD. The numerator is estimated from the power-law fit, while for the denominator we use the Hankel transform of the HaloFit [33] power spectrum as computed by CLASS [34] which is approximately a power-law on these scales.

We utilize clustering measurements from various surveys in the literature [23, 26–31]. Note that we adopt r_0 values from [23] for all surveys, as they have reported the values from the literature after normalizing for some methodology differences. We estimate b as described above for a range of redshifts (z) and flux limits (f_{lim}) and the results are shown in Fig. 1. For convenience we fit these results with

$$b(f_{\text{lim}}, z) = A(f_{\text{lim}})(1 + z) + B(f_{\text{lim}})(1 + z)^2 \quad (2.4)$$

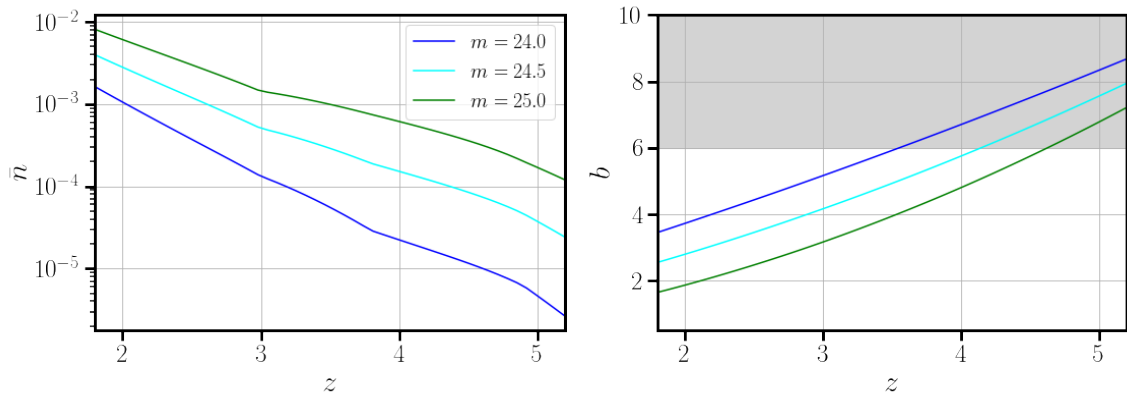


Figure 2: Left: Number density \bar{n} of LBGs using Schechter function fits to the UV LF [17], using fit parameters reported from preceding studies [36–38]. Right: Large-scale bias b of LBGs using a fit function $b(m, z)$ in Eq. 2.9 [17]. The region $b \geq 6$ is shaded to indicate that these high bias tracers are traditionally not used for cosmology.

where

$$A(f_{\text{lim}}) = 0.457 - 1.755(\log_{10} f_{\text{lim}} + 17) + 0.720(\log_{10} f_{\text{lim}} + 17)^2 \quad (2.5)$$

$$B(f_{\text{lim}}) = 0.012 + 0.318(\log_{10} f_{\text{lim}} + 17) + 0.043(\log_{10} f_{\text{lim}} + 17)^2 \quad (2.6)$$

are both quadratic functions of $\log_{10} f_{\text{lim}}$, with the flux measured in $\text{erg cm}^{-2} \text{s}^{-1}$ by standard convention. The shape of this fit is motivated by a similar fit to the LBG bias in ref. [17]. Since at these high redshifts the linear growth rate $D(z) \propto (1+z)$ the $(1+z)$ term corresponds to co-evolution [35] while the $(1+z)^2$ term is its first order correction. Ultimately, however, this is simply a convenient fit to the observed results. The solid lines in Fig. 1 show the fit for $f_{\text{lim}} = 3, 5$ and $10 \times 10^{-17} \text{ erg cm}^{-2} \text{ s}^{-1}$. Note that while we choose to model b as a function of f_{lim} , which can be derived from L_{lim} , it is common for surveys to report the limiting luminosity in terms of the median luminosity L_{med} . The conversion from L_{med} to L_{lim} , assuming a Schechter luminosity function, is described in Appendix B.

2.2 Lyman Break Galaxies

Lyman break galaxies (LBGs) [15–17] are a set of massive, actively star-forming galaxies at high redshift. The population is typically selected through a ‘dropout’ technique in which the selection targets the distinct drop in flux density F_ν that occurs at 912\AA (the Lyman break) due to absorption by stellar atmospheres and interstellar medium on top of an otherwise flat spectrum. For the redshifts of our interest, the spectra bluewards of 1216\AA is further suppressed due to Lyman-series blanketing [39]. Importantly, selection for this drop yields physically similar galaxies across redshift. Each selection sample is typically named after the filter that is used to detect this drop. For instance, a u -dropout sample will have a lack of flux in the u band compared to significant flux in redder bands, corresponding to galaxies at $z \approx 3$. The typical width for each sample is $\Delta z \approx 0.7$. Similar to LAEs, the number density \bar{n} and large scale bias b are our key parameters, allowing us to use a nearly identical approach for parameter estimation. The results are summarized in Figure 2.

z	2.2	2.5	3.1	3.9	4.7	5.4
LAE f_{lim}^*	13	11	5.6	5.1	5.4	6.9
z	2	–	3	3.8	4.9	5.9
LBG m^*	24.2	–	24.7	25.4	25.5	25.8

Table 1: Characteristic luminosity of Schechter function fits to the LAE LF [22] and LBG LFs [17] (in turn based on [36–38]), converted to line flux (in units of 10^{-17} erg cm $^{-2}$ s $^{-1}$) and apparent magnitude, respectively. This can be used to gauge what the optimal limiting luminosity is for experiments, as the LF will transition from an exponential to a power-law fainter than these characteristic luminosities and provide diminishing returns in galaxy counts.

The Schechter formalism is once again useful to predict the number density. Here, we will be using the UV ($\approx 1500\text{\AA}$ rest-frame) LF with absolute magnitude M_{UV}

$$dn(M_{\text{UV}}) = \left(\frac{\ln 10}{2.5}\right) \phi^* 10^{-0.4(1+\alpha)(M_{\text{UV}} - M_{\text{UV}}^*)} \exp\left\{-10^{-0.4(M_{\text{UV}} - M_{\text{UV}}^*)}\right\} dM_{\text{UV}} \quad (2.7)$$

with the LF parameters from Table 3 of ref. [17] (in turn based on refs. [36–38]). The absolute magnitude can be converted to apparent magnitude, m , using the appropriate (near-zero) k -correction [17]

$$M_{\text{UV}} = m - 5 \log_{10} \left(\frac{D_L(z)}{10\text{pc}}\right) + 2.5 \log_{10}(1+z) + \underbrace{m_{\text{UV}} - m}_{\approx 0} \quad (2.8)$$

We will use this to model (apparent) magnitude limited surveys.

The LBG biases are calculated using the same power-law approximation of correlation functions as in LAEs. Ref. [17] fit a function $b(m, z)$ to results from the literature

$$b(m, z) = A(m)(1+z) + B(m)(1+z)^2 \quad (2.9)$$

where $A(m) = -0.98(m - 25) + 0.11$ and $B(m) = 0.12(m - 25) + 0.17$. Again, while this fitting model has some physical basis on the co-evolution approximation of galaxies, it is ultimately a useful fit to the data.

The summary of the characteristic luminosities for LAEs and LBGs, shown in Table 1 provide us with an intuitive limit on where our gains are maximized when pushing to fainter luminosities. Starting at high luminosities, the number densities increase exponentially as we push fainter until we reach the “knee” at the characteristic luminosity (L^*), where the increase turns to a power-law. Near-term surveys will be able to reach such regimes.

For this work, we will consider a ‘Stage 4.5’ design motivated by the DESI II design with $2.4 < z < 3.2$, and a ‘Stage V’ design with $2.4 < z < 4.4$. The redshift ranges are inspired by existing survey designs [9] and ongoing work by DECam probing LAEs up to $z \sim 4.5$ [21]. Both designs are constrained by the limiting luminosities for LAEs and LBGs. While Stage 4.5, with a closer timeline, is specified in luminosity limits, we will consider multiple scenarios of Stage V luminosity limits to perform a crude optimization. The optimization will be done by assuming both a fixed total integration time for the experiment and a fixed individual integration time per galaxy, regardless of flux, magnitude, or galaxy type. This is equivalent to fixing the total number of galaxies observed and we achieve this

Experiment	$2.4 < z < 3.2$		$3.2 < z < 4.4$		$N [1/\text{deg}^2]$		f_{sky}
	f_{lim}	m	f_{lim}	m	LAE	LBG	
Stage 4.5	10	24.5	–	–	489	1237	0.1212
Stage V Plan A	10	24.5	10	24.5	611	1716	0.4
Stage V Plan B	10	24.5	5	24.5	1294	1716	0.3092
Stage V Plan C	10	24.5	10	25.0	611	2959	0.2607

Table 2: Experiment designs considered for this work. f_{lim} and m refer to the limiting flux of LAE samples and limiting apparent magnitude of LBG samples, respectively. The units of f_{lim} are $10^{-17} \text{erg/cm}^2/\text{s}$. The Stage 4.5 design is strongly motivated by the proposed DESI II design.

by tuning f_{sky} for each Stage V design to counteract change in number density by the choice of luminosity limits. The experimental designs are shown in Table 2. Note that these designs are exploratory by nature, as neither the capabilities of next-generation facilities nor tracer characteristics are determined and will benefit from a forecast with broad considerations rather than precise optimization. A comparison against Table 1 shows that for a Stage 4.5 survey with $f_{\text{lim}} = 10 \times 10^{-17}$, $m = 24.5$, and $z \lesssim 3$, the luminosity limits are near the characteristic luminosities with the exception of LAEs at $z = 3.1$.

A more quantitative measure of the strength of our signal is where in k -space we become shot noise limited in the monopole, as shown in Figure 3. For the Stage 4.5 survey, the LAE signals become shot noise limited at $k \simeq 0.15 h \text{Mpc}^{-1}$ and LBGs at $k \simeq 0.3 - 0.4 h \text{Mpc}^{-1}$. Furthermore, if we extend these luminosity limits to $z = 4$, we are totally shot noise dominated for LAEs. Notice that the magnitude limits on the right axis do not go to 26 for $z = 2.5$ and 3.0. This is because the bias-corrected shot noise $[\bar{n}(b^2 + 2bf/3 + f^2/5)]^{-1}$ increases at fainter magnitudes due to the decrease in bias over-powering the increase in number density as we push fainter than the corresponding characteristic magnitudes of the LBG Schechter function fit.

2.3 CMB Lensing

We will also include CMB lensing κ as a third tracer of the matter density. The aspect of lensing that makes it a particularly interesting addition to the set of tracers is that it introduces fewer nuisance parameters than a galaxy tracer; it is an unbiased tracer of matter, with no shot noise. The high redshifts of near-term experiments further motivate the use of lensing, as the CMB lensing kernel peaks near these redshifts. On the other hand, we will not be including cosmic shear as a tracer, as this will require galaxy sources at extremely high redshift. Refer to Figure 4 for the full redshift overlap between density tracers considered for this work.

We consider Simons Observatory (SO) [43] with $f_{\text{sky}} = 0.4$ as the CMB experiment for our forecasts and use the noise N_{ℓ}^{κ} obtained from the [SO noise calculator](#) as in ref. [5]. The calculator uses an iterated minimum variance (MV) quadratic estimator and MV internal linear combination of both CMB temperature and polarization data for calculation, and includes atmospheric effects [5].

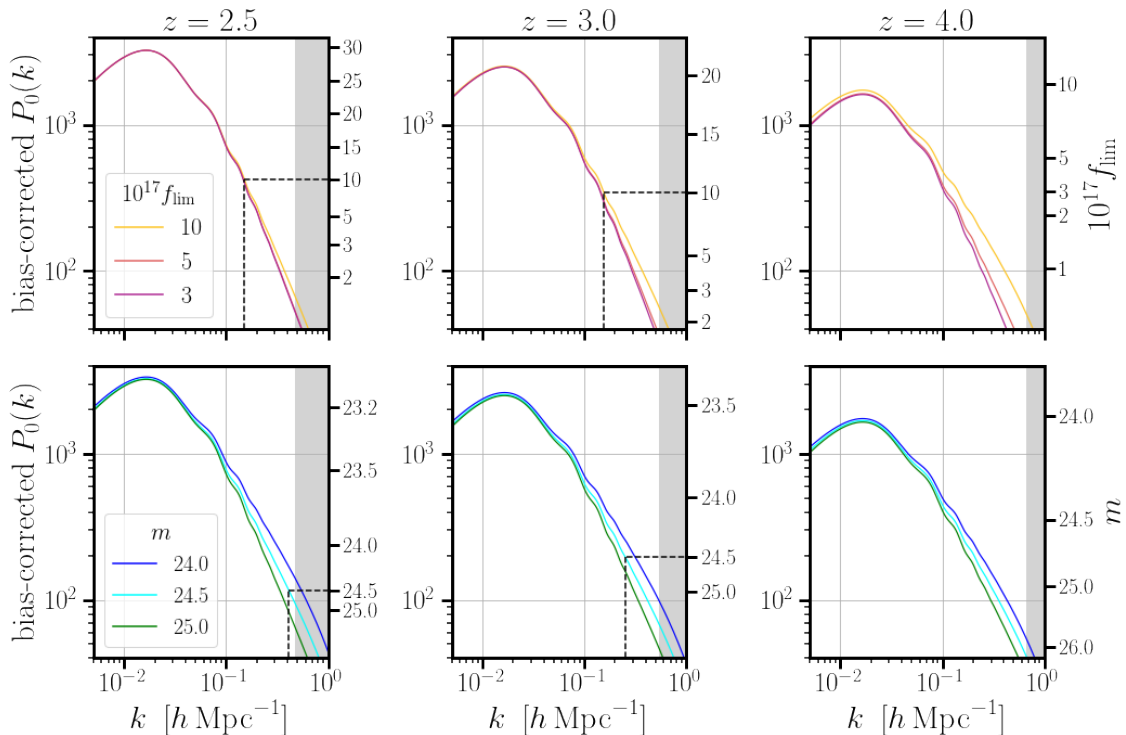


Figure 3: Monopole of the signal ($P - P_{\text{stoch}}$) against the shot noise at various luminosity limits (right axis) for LAEs (top) and LBGs (bottom). The k where signal equals shot noise reflects where we enter a shot noise dominated regime ($\bar{n}P=1$). The bias-correction simply refers to dividing out the monopole Kaiser factor, $b^2 + 2bf/3 + f^2/5$, so that the large-scale clustering is independent of magnitude. The spread in the curves at high- k is due to scale-dependent bias, which we model as described in §3. The dotted lines illustrate where the fiducial Stage 4.5 survey become shot noise dominated.

3 Theory and formalism

In this section we outline the theoretical models we employ and the forecasting formalism we adopt, which is based on the Fisher matrix and is substantially similar to that used¹ in ref. [5]. We take Λ CDM as our fiducial cosmology with parameters given in Table 3.

3.1 Model

As in ref. [5], our theoretical model is based upon 1-loop perturbation theory with a general, quadratic bias model. This model has been shown to be accurate (at the relevant scales) well beyond the demands of current and next-generation surveys [44] while including scale-dependent bias and mode-coupling due to quasi-linear evolution that improve the reliability of the forecasts. It has been applied to earlier surveys in ref. [45–47] and is currently being evaluated for use in the DESI and Euclid surveys [48]. For further details of the model see [44, 49, 50].

¹<https://github.com/NoahSailer/FishLSS>

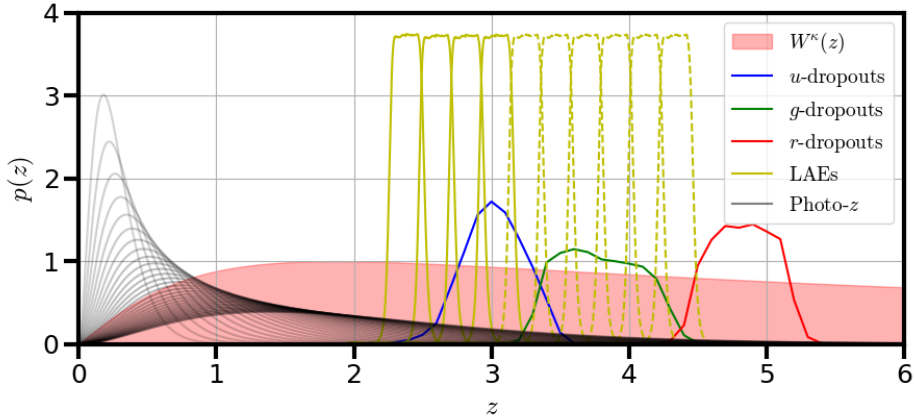


Figure 4: The normalized redshift distribution of the matter tracers considered for this work. The colored curves indicate the normalized redshift distribution of galaxy samples [17, 38, 40] observed by spectroscopic experiments in Table 2. The LAE filter limits for Stage 4.5 redshifts are inspired by an ongoing DECam medium-band survey [40] and extrapolated for higher redshifts. Note that the filters of LAE samples are not identical the redshift bins of the forecast. The light red region indicates the CMB lensing kernel $W^\kappa(z) \propto W^\kappa(\chi)/H(z)$ normalized to 1 at maximum. Also included is a common approximate distribution of magnitude limited samples in photometric surveys [17, 41, 42] that we do not forecast for in this work. The magnitude limits are $i_{\text{lim}} = 20, 20.5, \dots 35$, with the higher magnitude limit samples extending to higher redshift.

Within this formalism, the auto- or cross-spectra for our tracers can be written as a linear combination of different ‘basis’ spectra multiplied by bias coefficients, plus contributions from counterterms and stochastic terms:

$$P(k, \mu) = \sum_{X,Y} b_X b_Y P_{XY}(k, \mu) + P_{c.t.}(k, \mu) + P_{\text{stoch}}(k, \mu) \quad (3.1)$$

where $X, Y \in \{m, \delta_L, \delta_L^2, s_L^2, \nabla^2 \delta_L, \dots\}$ label the component spectra, $P_{c.t.}$ are counterterms arising from small-scale physics not directly included in the model, and P_{stoch} are stochastic terms such as shot noise and fingers of god. Figure 5 shows the contribution of each component in a sample case of constant biases, $b_a = 2$ and $b_b = 5$, constant number density, $\bar{n} = (100b^2)^{-1}$, and no correlation between the shot noise in the two samples (these assumptions correspond to $\tilde{N} = 100$ and $f_{\text{over}} = 0$, as introduced later in this section). Note how the scale and angle dependence of each component spectra differ, allowing us to potentially break degeneracies between parameters.

3.2 Parameters

The parameters that we use can be categorized into ‘global’ and ‘local’ parameters. The global parameters are those that are common to all redshifts, such as cosmological parameters. The local parameters are those that are assigned for each redshift that we consider. The perturbation theory parameters that we describe here (b_i, N_i, α_i) are examples of local parameters. For a complete list of parameters, their categorization (global or local), and their fiducial values, refer to Table 3.

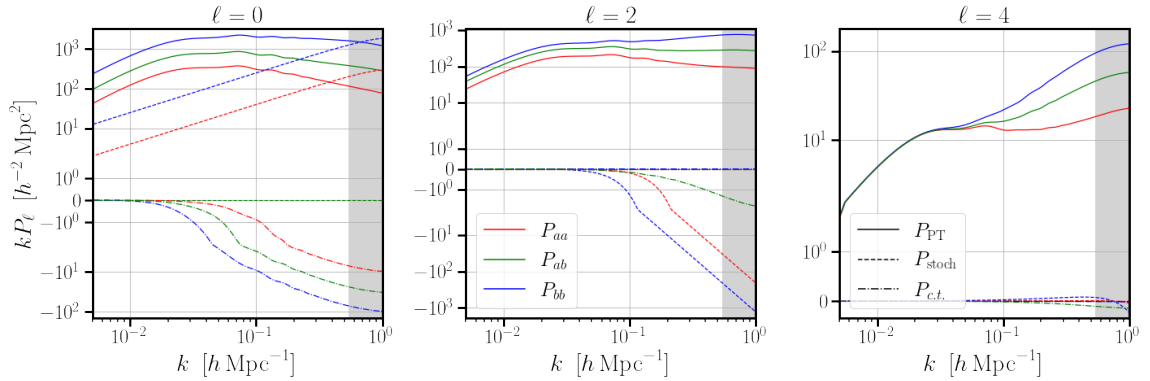


Figure 5: The contributions to the power spectra from each component in Eq. (3.1), where $b_a = 2$, $b_b = 5$, $z = 3$, and P_{PT} refers to the sum of quadratic bias component spectra $\sum_{X,Y} b_X b_Y P_{XY}(k, \mu)$. The columns refer to the monopole, quadrupole, and hexadecapole of each component. Red lines show the aa auto-spectra, green lines the ab cross-spectra, and blue lines the bb auto-spectra. The shaded region reflects the k_{nl} limit at $z = 3$.

The bias parameters b_X contribute to the spectra are organized in terms of the dependence of the galaxy overdensity field δ_g on the matter field δ and shear s_{ij} . Up to one-loop, the bias terms that we include in our model are

$$\delta_g = b_1 \delta + \frac{b_2}{2} \delta^2 + b_s s^2 \quad (3.2)$$

where $s^2 = (s_{ij})^2$ [49]. The cubic bias terms are nearly degenerate with our counter- and stochastic terms and so do not need to be included explicitly. This expression corresponds to the parametrization used in Eulerian perturbation theory (EPT). Each Eulerian bias can be related to the Lagrangian biases b_X^L as [11, 49]

$$b_1 = b_1^L + 1, \quad b_2 = b_2^L + \frac{8}{21} b_1^L, \quad b_s = b_s^L - \frac{2}{7} b_1^L \quad (3.3)$$

The fiducial values for each parameter is dependent on that of b_1 , which we have estimated for both LAEs and LBGs in §2. For b_2 , we use the Sheth-Tormen mass function [51] and peak-background split model, for which [52, 53]

$$b_1^L = \frac{1}{\delta_c} \left[a\nu^2 - 1 + \frac{2p}{1 + (a\nu^2)^p} \right] \quad (3.4)$$

$$b_2^L = \frac{1}{\delta_c^2} \left[a^2 \nu^4 - 3a\nu^2 + \frac{2p(2a\nu^2 + 2p - 1)}{1 + (a\nu^2)^p} \right] \quad (3.5)$$

with $\delta_c = 1.686$, $a = 0.707$ and $p = 0.3$. This is shown to agree well with N-body simulations for b_2 [54] and thus motivates a reasonable fiducial value for our samples. Furthermore, we have confirmed that our results are qualitatively invariant to our choice of b_2 . For b_s , we use the coevolution approximation, which assumes $b_s^L = 0$. While this does not agree as closely with simulations as our choice for b_2 , simulations suggest that for our samples we expect $|b_s^L| \lesssim 1$ [54], and the differences have little impact on our forecasts.

Our model for the counterterm consists of parameters $\alpha_{2n,a}$, such that

$$P_a \supset \alpha_{2n,a} \mu^{2n} (k/k_\star)^2 P_{cb} \quad (3.6)$$

for each auto-spectrum, with $k_* = 1 h \text{Mpc}^{-1}$. We inherit the fiducial values of galaxy α 's from ref. [5], where α_0 values are determined using fits towards Halofit simulations and higher order parameters are set to 0 for convenience. For $\alpha_{0,\kappa}$, we obtain fiducial values by simply fitting $P_{HF}(z) = P_{\text{lin}}(1 + \alpha_{0,\kappa}k^2)$. Cross-spectra counterterm contributions are fully determined by those of the auto-spectra, thus we do not have degrees of freedom for $\alpha_{ab,a \neq b}$, for example. A detailed discussion of cross-spectrum counterterms is provided in Appendix C.

For the stochastic terms, we use a set of parameters $N_{2n,ab}$, such that

$$P_{ab} \supset N_{2n,ab}(k\mu)^{2n} \quad (3.7)$$

Our fiducial values of the parameters are survey dependent for $n = 0$ or 1, and zero for higher orders. Note that $n = 0$ is the ‘‘shot noise term’’, and hence our fiducial value is $N_{0,aa} = 1/n_a$ for auto-spectra. Extending this model to cross-spectra, we let $N_{0,ab} = f_{\text{over}}/\sqrt{n_a n_b}$ fiducially for $a \neq b$, where $f_{\text{over}} \in [0, 1]$ is a measure of how much correlation we have between the tracers’ shot noise (e.g. to what degree the populations occupy the same halos). As the fiducial value for N_2 , we set $N_{2,ab} = -N_{0,ab}\sigma_v^2$, with $\sigma_v = (1+z)(100\text{km/s})/H(z)$ being the typical velocity dispersion in comoving units [5]. Notice that the stochastic parameters are the only new degrees of freedom introduced when including the cross-spectra, motivating the use of all available spectra.

Our k_{max} is set by the non-linear scale. Unless explicitly stated, we will use $k_{\text{max}}(z) = k_{\text{nl}}(z) = \Sigma^{-1}(z)$ where Σ is the rms displacement in the Zel’dovich approximation. We take $k_{\text{min}} = 0.003 h \text{Mpc}^{-1}$, motivated by the longest mode that fit in our surveys, i.e. $k_{\text{min}} \sim 2\pi/V^{1/3}$. Our results are in general not very sensitive to k_{min} .

3.3 2D power spectrum

To include CMB lensing in our analysis, we must also have a method to calculate the 2D power-spectra, where we can cross-examine the LSS and CMB data on equal footing. The 2D power-spectra can be calculated from the 3D power-spectra using the Limber approximation,

$$C_\ell^{ab} = \int_0^{\chi_*} d\chi \frac{W^a(\chi)W^b(\chi)}{\chi^2} P_{ab} \left(k_\perp = \frac{\ell + 1/2}{\chi}, k_\parallel = 0 \right) \quad (3.8)$$

where the a and b are available tracers, either κ or galaxies. χ_* is the comoving distance to the surface of last scattering and W 's are the lensing kernels

$$W^\kappa(\chi) = \frac{3}{2}\Omega_m H_0^2(1+z) \frac{\chi(\chi_* - \chi)}{\chi_*} \quad \text{and} \quad W^{g_a}(\chi) \propto H(z) \frac{dN_a}{dz} \quad (3.9)$$

where W^g is normalized such that $\int_\chi W^g(\chi) = 1$. Note that we take the lowest order correction to the Limber approximation $\ell \rightarrow \ell + 1/2$, improving our precision to $\mathcal{O}(\ell^{-2})$ [5, 55]. We do not marginalize over higher order stochastic and counter-term parameters for the 2D power-spectra, as the Limber approximation limits us to $\mu = 0$. For the lensing-lensing auto-spectrum, the ℓ_{max} is limited not by k_{nl} , but by a stricter constraint from baryonic feedback, which limits us to $\ell < 500$. For the rest of the spectra, we translate our k_{max} constraints into ℓ_{max} .

3.4 Fisher formalism

The Fisher matrix formalism [56] allows us to forecast the parameter constraints on an assumed underlying model, given a experimental configuration. It is widely used to understand the impact of survey design choices and parameter degeneracies on the inference of cosmological parameters [5, 57–61]. The Fisher matrix can be calculated as

$$F_{ij} = \sum_{X,Y} \int \frac{k^2 dk d\mu}{2\pi^2} \frac{\partial P_X}{\partial \theta_i} \mathbf{C}_{XY}^{-1} \frac{\partial P_Y}{\partial \theta_j} \quad (3.10)$$

where X, Y label available auto- and cross-spectra, θ_i are parameters, $\mathbf{C}_{XY}^{-1} = (\mathbf{C}^{-1})_{XY}$ and the covariance matrix \mathbf{C} is

$$\mathbf{C}_{abcd} = P_{ac}P_{bd} + P_{ad}P_{bc} \quad (3.11)$$

where the subscripts represent the samples used to calculate spectra. Note that the power-spectra (P_X, P_{ab}) above include the counter and stochastic terms. We compute these matrices using the FishLSS code, which was originally developed for single-tracer forecasts [5] and extended to multitracer forecasts for this work. In the development process we have confirmed that the new version of the code reproduces previous results in single-tracer cases. Without full consideration of multi-tracer effects, one would calculate the Fisher matrix with X, Y summing over only the auto-spectra and thus lose information gained from the cross-spectra.

For a general galaxy-galaxy-lensing sample, the formalism is modified slightly. While the Fisher matrix earlier still holds, one must compute the matrix using the angular power-spectra C_ℓ^X as well. One obtains the full set of information by combining the Fisher matrices from the 3D power-spectra and 2D power-spectra. By restricting the full-shape signal to $k_\parallel > 10^{-3}$, there will be no covariance between the full-shape and the angular spectra that probe $k_\parallel \sim 0$. This will allow for the Fisher matrices to simply add together [5, 56].

The covariance matrix for a galaxy-galaxy-lensing cross-analysis is

$$(\mathbf{C}_\ell)_{XY} = \begin{cases} 2(C_\ell^{\kappa\kappa} + N_\ell^{\kappa\kappa})^2 / f_{\text{sky}}^{\text{CMB}} & X = Y = \kappa\kappa \\ (C_\ell^{\kappa g_{a,i}} C_\ell^{\kappa g_{b,j}} + \delta_{ij} (C_\ell^{\kappa\kappa} + N_\ell^{\kappa\kappa}) C_\ell^{g_{a,i} g_{b,i}}) / f_{\text{sky}}^\cap & X = \kappa g_{a,i}, Y = \kappa g_{b,j} \\ \delta_{ij} (C_\ell^{g_{a,i} g_{c,i}} C_\ell^{g_{b,i} g_{d,i}} + C_\ell^{g_{a,i} g_{d,i}} C_\ell^{g_{b,i} g_{c,i}}) / f_{\text{sky}}^{\text{LSS}} & X = g_{a,i} g_{b,i}, Y = g_{c,i} g_{d,i} \\ 2(C_\ell^{\kappa\kappa} + N_\ell^{\kappa\kappa}) C_\ell^{\kappa g_{a,i}} / f_{\text{sky}}^{\text{CMB}} & X = \kappa\kappa, Y = \kappa g_{a,i} \\ 2C_\ell^{\kappa g_{a,i}} C_\ell^{\kappa g_{b,i}} f_{\text{sky}}^\cap / (f_{\text{sky}}^{\text{CMB}} f_{\text{sky}}^{\text{LSS}}) & X = \kappa\kappa, Y = g_{a,i} g_{b,i} \\ \delta_{ij} (C_\ell^{\kappa g_{b,i}} C_\ell^{g_{a,i} g_{c,i}} + C_\ell^{\kappa g_{c,i}} C_\ell^{g_{a,i} g_{b,i}}) / f_{\text{sky}}^{\text{LSS}} & X = \kappa g_{a,i}, Y = g_{b,i} g_{c,i} \end{cases} \quad (3.12)$$

and the Fisher matrix is

$$F_{ij}^{2D} = \sum_{\ell=\ell_{\min}}^{\ell_{\max}} (2\ell + 1) \sum_{XY} \frac{\partial C_\ell^X}{\partial \theta_i} (\mathbf{C}_\ell)_{XY}^{-1} \frac{\partial C_\ell^Y}{\partial \theta_j} \quad (3.13)$$

where f_{sky}^\cap is the overlapping sky area between LSS and CMB surveys, and X, Y sum over the available spectrum $\{\kappa\kappa, \kappa g_{a,i}, g_{a,i} g_{b,i}\}$ for all available galaxy tracers a, b and redshift bins i [5]. For the purposes of our forecast we assume maximal overlap between LSS and CMB experiments, i.e. $f_{\text{sky}}^\cap = \min(f_{\text{sky}}^{\text{CMB}}, f_{\text{sky}}^{\text{LSS}})$. Note that the cross-spectra between tracers at different redshift bins is zero, so we do not sum over them.

The simple treatment of priors is a strength of the Fisher formalism, with the inverse covariance of the priors simply treated as an added information matrix. We will be using conservative priors on the nuisance parameters to regularize forecast behavior. The set of

priors used is shown in Table 4. Most of the nuisance parameter priors reflect the fidelity we have on constraining these parameters, by applying uncertainties proportional to their fiducial value. This cannot be done for parameters with a fiducial value of 0, so we describe this briefly. For $N_{ab,a\neq b}$ and $N_{2,ab,a\neq b}$, we apply the same errors as those of the auto-spectra, assuming there is full correlation between the shot noise of two galaxy populations (e.g. $N_{ab,a\neq b} = 1/\sqrt{n_a n_b}$). The other terms with fiducial value have no prior, due to the lack of conservative expectation for their values. We have confirmed that our conservative priors have little effect on our final results. We will be considering both BBN and Planck priors for cosmological parameters.

3.5 Benefits of multi-tracer cosmology

The use of multiple tracers is closely associated with the idea of ‘sample variance cancellation’ [12, 62]. For two quantities, e.g. a density and velocity field, some relationships can be measured at the field level and thus do not pay any sample variance penalty. For example, within linear theory and in general relativity, the density contrast $\delta(\mathbf{k})$ is related to the velocity divergence, $\theta(\mathbf{k})$ mode-by-mode. A ratio of measured modes can thus measure f with no sample variance penalty. Similarly, for linear theory and scale-independent, deterministic bias the ratio of $\delta_i(\mathbf{k})$ for two galaxy samples measures the ratio of their biases in a way that is not limited by sample variance. Colloquially we say that sample variance has ‘canceled’, though it would be more correct to state that sample variance only enters when comparing a particular realization to the ensemble average. While in general, cosmology dependence enters quantities (such as the linear power spectrum) that are expectation values, for some situations (such as the scale-dependent bias introduced by primordial non-Gaussianity) this is not the case and ‘cancellation’ can lead to tremendous gains in precision.

Sample variance cancellation can be recast as a fitting problem, in which case it becomes the statement that when including cross-correlations in addition to auto-correlations noise that is highly correlated between probes does not get double counted [59]. In such situations some eigenvectors ‘pay’ the sample variance penalty while others do not.

Past applications of sample variance cancellation [63] have not found drastic gains in constraining power from easily achievable number densities and we are unlikely to have high-enough number densities for this either. However, another use of multiple tracers is to break degeneracies between parameters. Including multiple tracers allow us to distinguish between parameter dependencies of the data, breaking parameter degeneracies that limit our precision. Recent studies indicate that in a general case, it is this degeneracy breaking that drives the improvements in constraints, rather than sample variance cancellation [64, 65].

4 Multitracer

Before we turn to forecasts for particular models let us investigate some test samples with semi-realistic parameters to gain a better understanding of the multitracer approach. To do this, we make forecasts for the amplitude of the linear theory power spectrum, σ_8 , holding fixed the other Λ CDM parameters $\{h, \tau, n_s, \omega_c, \omega_b\}$ at some fiducial values. We allow the biases, counterterms and stochastic terms for each sample to vary.

Throughout this section we use the notation a and b to refer to the auto-spectrum analyses of each tracer, “auto” or $aa + bb$ refers to using two tracer populations, but with only the galaxy auto-spectra considered (i.e. incomplete multitracer) and “full” or $a \times b$ refers to the complete multitracer approach including the galaxy-galaxy cross-spectrum.

Parameter	Definition	Fiducial value
$\log A_s$	Primordial amplitude	2.10732×10^{-9}
n_s	Spectral index	0.96824
h	Hubble parameter: $H_0/100$ km/s/Mpc	0.6770
τ	Optical depth to reionization	0.0568
ω_c	fractional dark matter density: $\Omega_c h^2$	0.11923
ω_b	fractional baryonic matter density: $\Omega_b h^2$	0.02247
b	First order bias $\delta_g \supset b_g \delta_m$	b_{LAE} : Eq. 2.4 b_{LBG} : Eq. 2.9 [17]
b_2	Second order bias	Eq. 3.5
b_s	Shear bias	$-\frac{2}{7}(b_g - 1)$
α_0	Lowest order counter term $P_{aa} \supset \alpha_{0,a} k^2 P_m$	$1.22 + 0.24 b_a^2 (z - 5.96)$
α_{2n}	Higher order counter terms $P_{aa} \supset \alpha_{2n,a} \mu^{2n} k^2 P_m$	0
N_{ab}	Shot noise term $P_{ab} \supset N_{ab}$	$N_{aa} = 1/\bar{n}_a$ $N_{ab, a \neq b} = 0$
$N_{2,ab}$	FOG-like effect $P_{ab} \supset N_{2,ab} (k\mu)^2$	$-N_{ab} \sigma_v^2$
$N_{4,ab}$	FOG-like effect $P_{ab} \supset N_{4,ab} (k\mu)^4$	0

Table 3: The parameters for our fiducial cosmological model, Λ CDM with massive neutrinos. The cosmological parameters are placed on the top and model parameters are on the bottom. The model parameters are individually assigned either to each tracer or each spectra. Furthermore, we allow model parameters to evolve over redshift, which gives us new degrees of freedom for each additional z bin.

Parameter	Uncertainty	Parameter	Uncertainty	Parameter	Uncertainty
b	100%	N_{aa}	100%	α_0	100%
b_2	100%	$N_{ab, a \neq b}$	$\sqrt{N_{aa} N_{bb}}$	α_2	∞
b_s	100%	$N_{2,aa}$	300%	α_4	∞
N_4	∞	$N_{2,ab, a \neq b}$	$3\sqrt{N_{2,aa} N_{2,bb}}$		

Table 4: Prior uncertainties for nuisance parameters. For Λ CDM parameters, we use BBN or CMB primary priors appropriately.

4.1 Linear

We will start by investigating multitracer cosmology in the Fisher formalism using linear theory. In linear theory, with the exception of shot noise, the power spectra of each galaxy population is proportional to the linear matter power spectrum

$$P_{ab}(k, \mu) = (b_a + f\mu^2)(b_b + f\mu^2)P_L(k) + N_{ab} \quad (4.1)$$

where b is the (deterministic, scale-independent) linear bias, f is the scale-independent growth factor, P_L is the linear theory matter power spectrum, N_{ab} is the shot noise term, and μ is the cosine of the angle to the line of sight. The relevant derivatives for linear theory power

spectrum are expressed as

$$\begin{aligned}\frac{\partial P_{ab}}{\partial \log \sigma_8} &= 2(b_a + f\mu^2)(b_b + f\mu^2)P_L \\ \frac{\partial P_{ab}}{\partial b_c} &= [\delta_{ac}(b_b + f\mu^2) + \delta_{bc}(b_a + f\mu^2)]P_L \\ \frac{\partial P_{ab}}{\partial N_{cd}} &= \delta_{ab,cd}\end{aligned}\tag{4.2}$$

We use this method first as a check on our code (since the calculation can be done analytically) and second to illustrate some of the features of multitracer cosmology.

The Fisher information is a function of both the amount of data and the degeneracy between the derivatives of the data with respect to the parameters. In multitracer cosmology, we hope to see an increase in constraints that goes beyond the simple increase in data quantity, which must come from breaking of degeneracy. However, in linear theory, the lack of parameter dependencies beyond the σ_8 - b degeneracy suggests that this will not occur.

At the minimum, we expect the low-bias tracer to improve the constraints by a significant margin, as low-bias tracers have an inherent advantage in constraining structure growth compared to high-bias tracers. Even if there is no synergy between the measurement, matching the low-bias constraints will significantly reduce the error from having a single, high-bias tracer. This can easily be explained in the following sense. In linear theory, the auto-spectrum of a biased tracer is given by

$$P(k, \mu) = (b + f\mu^2)^2 P_L(k) + N = (b\sigma_8 + f\sigma_8\mu^2)^2 \hat{P}_L(k) + N\tag{4.3}$$

where \hat{P}_L is the normalized linear power-spectrum, $P_L = \sigma_8^2 \hat{P}_L$. As b is a nuisance parameter, one must probe for the μ -dependence of the spectrum to obtain σ_8 . With the error proportional to the overall spectrum mode-by-mode ($\delta P \propto P$), one loses constraining power on σ_8 with greater b . To maximize SNR, it's clear that we must minimize b and maximize \bar{n} , both of which are satisfied by choosing a low-bias sample. In the limit that we go to $b = 0$, we are measuring the velocity divergence θ . In this case, our precision of the amplitude of P is sample variance limited such that $\delta A/A = \sqrt{2/N_{\text{modes}}}$, making $\delta\sigma_8/\sigma_8 = (1/2)\sqrt{2/N_{\text{modes}}}$.

Before proceeding further, let us define an effective shot noise \tilde{N} , as

$$b^2 \tilde{N} \equiv \frac{1}{\bar{n}}\tag{4.4}$$

We will use \tilde{N} to explore different noise regimes throughout this section. For reference, at $z = 3$, LAEs with f_{lim} of 3, 5, $10 \times 10^{-17} \text{ erg cm}^{-2} \text{ s}^{-1}$ have $\tilde{N} \approx 100, 170, 410$, and LBGs with $m = 24, 24.5, 25$ have $\tilde{N} \approx 570, 230, 140$, respectively, in units of $h^3 \text{ Mpc}^{-3}$.

Let us consider samples in linear theory, with constant biases, $b_a = \{1.5, 2, 3, 4\}$, $b_b = 5$, and a linear regime $k_{\text{max}} = 0.1 h \text{ Mpc}^{-1}$. A subset of our constraint calculations are shown in Figure 6. As we predict there is little to no improvement from adding the cross-spectrum, as shown in Figure 7, indicating that we are losing little to degeneracy.

In the same figure, we detect that the ‘auto’ ($aa+bb$) results are significantly better than the single low-bias result. This indicates that a naive error propagation of $1/\sigma^2 = 1/\sigma_1^2 + 1/\sigma_2^2$ is not appropriate, as this predicts the low-bias and ‘auto’ constraints to be similar for most of our samples. The reason is that we must include the correlation between measurements

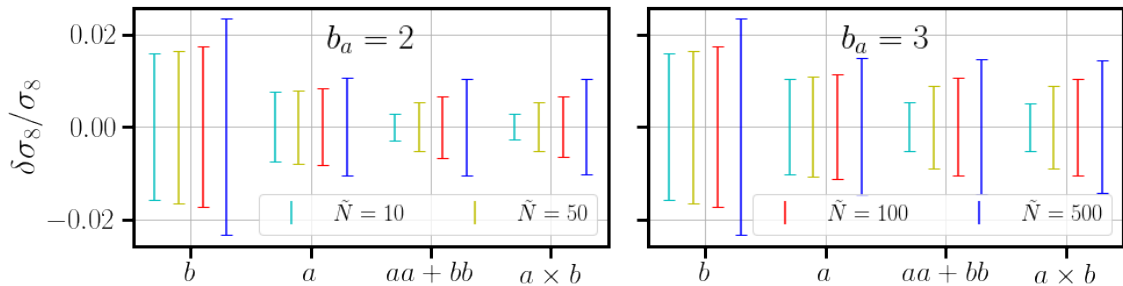


Figure 6: The relative constraints of σ_8 computed in linear theory, with constant linear biases and number densities. $\tilde{N} = (b^2\bar{n})^{-1}$ is the effective shot noise. a and b refer to the one-tracer constraints from each tracer, $aa + bb$ refer to the auto-spectra (incomplete multitracer) constraints, and $a \times b$ refer to the complete multitracer constraint.

(e.g. the velocity part of the power spectra is the same). Including the correlation, r , the variance σ^2 becomes

$$\sigma^2 = \frac{(1 - r^2)\sigma_1^2\sigma_2^2}{\sigma_1^2 - 2r\sigma_1\sigma_2 + \sigma_2^2} \quad (4.5)$$

for the composite measurement, with σ_i referring to the uncertainty of the i 'th measurement. Refer to Appendix A for detailed calculations.

This result explains the two main trends that we see. The first trend, the decreasing improvement as one takes $b_a \rightarrow b_b$, can be illustrated by the case with redundant measurements ($\sigma_1 = \sigma_2$, $r \rightarrow 1$), which yields $\sigma^2 = \sigma_1^2 = \sigma_2^2$. The second trend, the increasing improvement as one goes to lower noise, follows the limit of non-redundant measurements with high correlation ($\sigma_1 \neq \sigma_2$, $|r| \rightarrow 1$), which yields $\sigma^2 \rightarrow 0$.

One can directly compare the $\delta\sigma_8/\sigma_8$ results with improvements in constraints for the linear bias ratio b_a/b_b , where sample variance cancellation is present [12]. A direct comparison is made in Figure 7. The lack of improvement in $\delta \log \sigma_8$ by including the cross-correlation, as compared to the significant improvement in $\delta(b_a/b_b)$, illustrates that sample variance cancellation is not relevant for constraining σ_8 .

4.2 Nonlinear

Now let us study the nonlinear scenario, with the fully general power spectrum (Eq. 3.1). The existence of many more parameters allows for the existence of significant parameter degeneracies, and hence the potential for significant degeneracy breaking from multitracer techniques. We test on samples of identical linear biases and noise to the linear regime examples, but with further analysis including CMB lensing as well.

A subset of the results are shown in Figure 8. For some samples there is visible improvement of constraints from adding the ab cross-spectrum, contrary to the marginal improvement seen in the linear regime. This indicates that we have degeneracy breaking at hand, as the test case in the linear regime has shown that the increase in information from the additional spectrum only improves our constraints marginally. The average improvement in constraining power by adding the cross-spectrum (auto \rightarrow full), which can be interpreted as the average degeneracy breaking, is 17%. This marks a 22% improvement from the low-bias tracer a and a 68% improvement from the high-bias tracer b . This effect of degeneracy breaking can vary

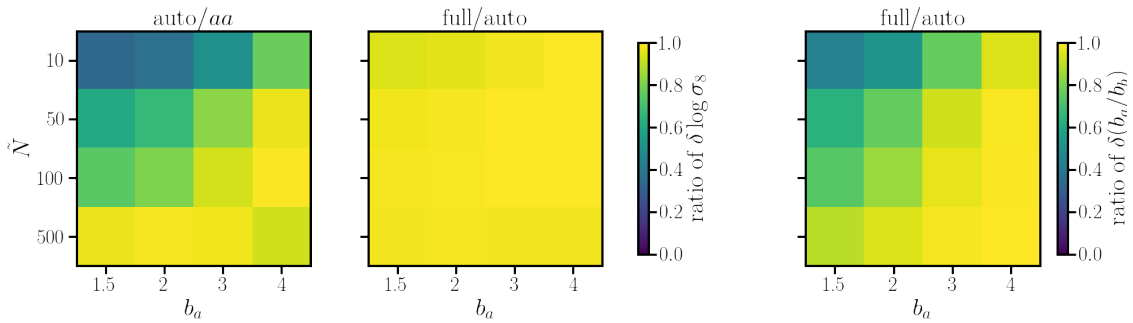


Figure 7: Left: Showing improvement in relative constraints of σ_8 , when including the high bias tracer to the low bias (auto/aa) and including cross-spectrum to auto-spectra (full/auto). Right: Showing improvement in relative constraints of b_a/b_b when including cross-spectrum to auto-spectra (full/auto). The significant improvement in $\delta(b_a/b_b)$ compared to $\delta \log \sigma_8$ show the power of sample variance cancellation where present.

significantly with the noise regime that we are working in. For instance, at $\tilde{N} = 10$ the improvement from auto \rightarrow full is 30% on average, while at $\tilde{N} = 500$ it is only 5%.

One can hope to further improve these results by reducing the number of added free parameters. A common practice in the field is to neglect the cross-spectrum stochastic terms $N_{2n,ab}$, by assuming that the two galaxy tracers have completely disjoint inhabitation of halos. While past work has shown that the inclusion of these parameters do not crucially change the forecast behavior [65], it will be worthwhile to investigate this further by considering small-scale cross-clustering of LBGs and LAEs at the redshifts and luminosities of relevance to future cosmology surveys.

From the perspective of added parameter space, the lack of new parameters other than $\alpha_{0,\kappa}$ makes CMB lensing an ideal candidate for cross-analysis. Our results, also shown in Figure 8, indicate that we have 11% improvement on average when adding lensing to our full multitracer case. When adding to each one-tracer case, we see a 6% improvement and 19% improvement for tracers a and b , respectively. Although the increments are significantly less than that of the galaxy-galaxy multitracer analysis, it is worthwhile to note that there is still improvement from lensing after including two galaxy tracers. We may attribute the little improvement from lensing to the limitations placed on the number of modes measured in a 2D power-spectrum, which is significantly less than that of the 3D spectrum, and the lack of cosmological parameters in this “fixed-shape” approach.

5 Radiative transfer

Radiative transfer (RT) is a known, yet unresolved potential cause of concern for the use of LAEs as matter density tracers. Ref. [66] suggests that RT can significantly vary the number of galaxies in catalog depending on the local density and LOS velocity divergence. The latter effect is degenerate with the μ dependence used to constrain $f\sigma_8$ in RSD studies (refer to §4 for a brief discussion in linear theory). A more recent work [67] argues that the limited resolution of early simulations are the source of such a large effect. Simulations with higher resolution show that regions of Ly α emission tend to have higher density, such that the photons escaping the galaxy have shifted further away from resonance and thus are

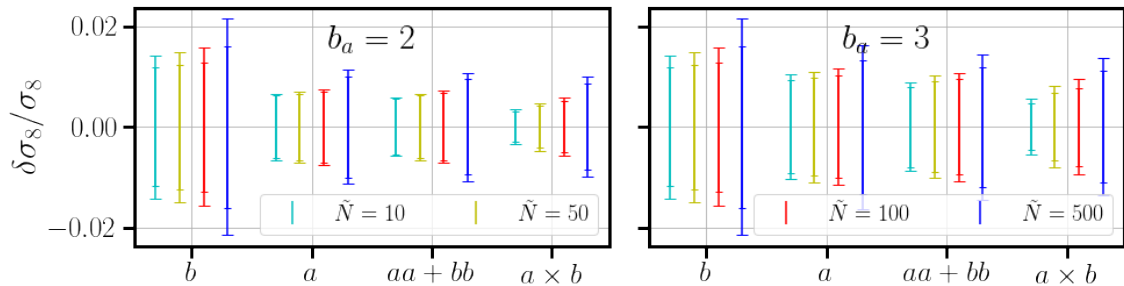


Figure 8: The relative constraints of σ_8 in the nonlinear regime, with various noise and b_a values. The constraints with smaller caps show the respective constraints including lensing.

less susceptible to scattering by the surrounding environment. While direct observations of RT effect are currently unavailable, the impact of HI absorption on LAE clustering has been detected [68].

For an analysis using only LAEs, a large RT contribution to the selection of galaxies would lead to very large errors on σ_8 . However, with a complex model that can potentially break degeneracies through multi-tracers, these samples may prove to be useful. In order to make a preliminary investigation of whether RT-affected tracers can still be valuable in multi-tracers, we take the following approach. We imagine that the RT effect is small enough that it can be included by taking

$$P(k, \mu) \rightarrow P(k, \mu) + 2\delta f (b\mu^2 + f\mu^4) P_L + \mathcal{O}(\delta f^2) \quad (5.1)$$

while leaving the higher loop terms unchanged. In principle there are corrections to all of the higher order biases and the 1-loop terms as well, but we are assuming that these terms are sub-dominant and multiplied by a “small” RT effect and thus they can be neglected. A more complete and consistent calculation will be attempted in a future publication.

6 Results

In this section we outline our main forecast results for two experiment designs: ‘Stage 4.5’, motivated by DESI II, and ‘Stage V’. As discussed in §2 we will use one luminosity limit ($f_{\text{lim}} = 10 \times 10^{-17}$ for LAEs and $m = 24.5$ for LBGs) as the fiducial design for Stage 4.5 and consider multiple scenarios of Stage V luminosity limits for a preliminary optimization constrained on the total number of galaxies observed. The experimental designs are shown in Table 2.

In this section, we will consider gains from any additional tracer as “multi-tracer improvement”, e.g. improvements from LBG-only analysis to an LAE \times LBG or $\kappa \times$ LBG analysis. This is unlike §4 where the focus was on the improvement gained through the inclusion of cross-spectra, and hence now the appropriate cross-spectra are always included when multiple tracers are in use. It should not be a surprise, however, that an inclusion of additional tracer improves the constraints with all else unchanged. To distinguish the gains from multi-tracer from the simple increment in data, we will be adjusting the number density of the LBG data available when including LAEs. The constraint here will be the total number of galaxies observed, as we have done when deciding the optimization for Stage V. As we have

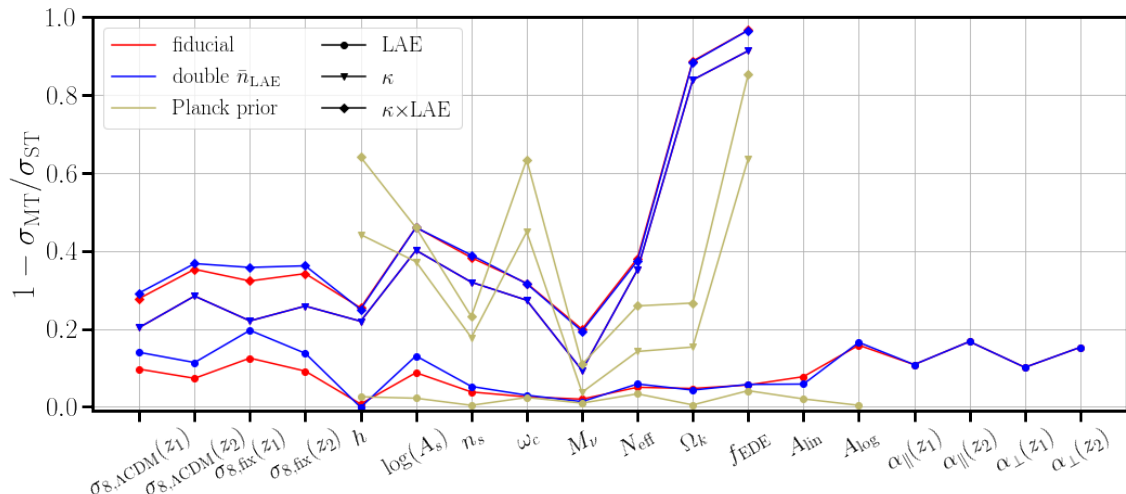


Figure 9: A summary of parameter constraint improvements from using multitracers in the Stage 4.5 design. The ‘ST’ and ‘MT’ on the y-axis refer to single tracer and multitracers, where the LBG-only sample is considered the base single tracer sample. The type of marker depicts what tracer was added on to the sample. The shown improvements for f_{EDE} , A_{lin} , A_{log} are the average improvements across the parameter space probed.

shown in Figure 5 that LBGs are less shot-noise dominated with existing luminosity cuts and the number density of LAEs are several factors smaller than LBGs, we will observe LAEs at maximum efficiency and decrease the LBG observation efficiency necessarily, to 0.61 (note that these efficiencies are multiplied by the 50% success rate for redshift detection that is always in place)². A similar treatment cannot be made for lensing as they are provided by CMB surveys separate from LSS experiments. Hence, we will compare the galaxy-only and $\kappa \times$ galaxy with the same galaxy samples and for this reason the LAE and lensing multitracers improvements should not be regarded on the same basis.

For all forecasts using full shape information, we include all relevant Λ CDM and nuisance parameters (Table 3) and treat extra parameters of interest as one parameter extensions. For cosmological priors, we will use conservative BBN priors of $\sigma(\omega_b) = 0.0005$ or CMB primary priors from Planck. A summary of the multi-tracers improvement in the Stage 4.5 design are provided in Figure 9.

The blue curve in the figure shows a case for when LAE number densities are doubled, in the BBN prior scenario. This is to address the concern raised in §2.1 that offsets of factor 2 on LAE number density estimates are not unlikely. The results illustrate that there are no qualitative changes to the final results.

6.1 Growth rate

In this section, we measure structure growth by measuring σ_8 constraints. While σ_8 is a well-motivated variable to pursue in multi-tracers both in terms of existing tensions in the field and linear theory arguments provided in §4, it is also a variable where we expect

²We have confirmed that the lack of inclusion of this LBG efficiency decrease affects the improvement results by $< 10\%$

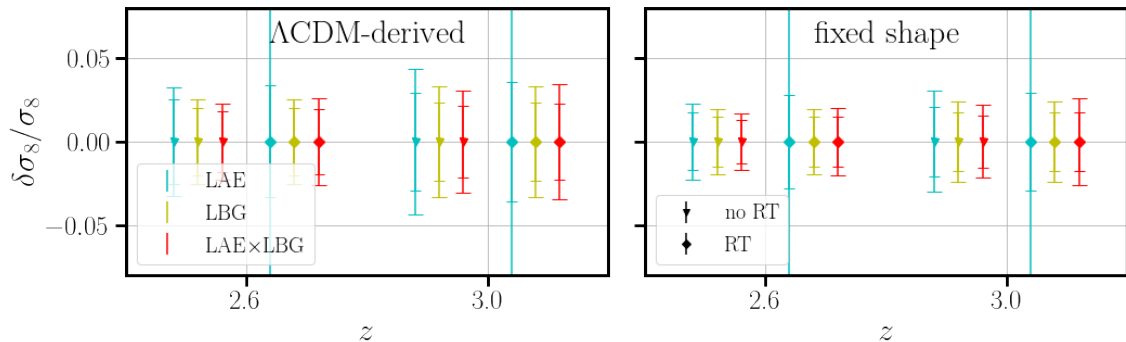


Figure 10: Relative constraints on $\sigma_8(z)$ from Stage 4.5 in the Λ CDM-derived (left) and fixed shape (right) methods. The smaller cap sizes correspond to the constraints including lensing. We see that the inclusion of RT effects diminish majority of the improvement from including LAEs.

significant impact from RT effects as mentioned in §5. It is possible that multi-tracers break the RT-induced degeneracies enough such that inclusion of LAEs significantly improve σ_8 constraints.

We use two approaches in this section. First we have our full-shape approach, which marginalizes over all of the Λ CDM parameters. Another approach is to use the ‘fixed-shape’ approach of §4, which takes a model-agnostic approach and only marginalizes over amplitude. The latter approach marginalizes over a subset of the former approach’s parameters and thus always yields tighter constraints. In both approaches, the lensing auto-spectrum is not included. This ensures that the $\sigma_8(z)$ constraints are local, using only the data collected in each redshift bin up to the shared BBN prior.

The results for Stage 4.5 are shown in Figure 10. We find that the both approaches gain $\approx 10\%$ from the introduction of LAEs. This is less than the improvements from including lensing, which are $\approx 20 - 30\%$. These improvements in total amount to $\approx 25 - 35\%$. Notice that unlike in §4, the low bias tracer LAE do not have tighter σ_8 constraints than the high bias tracer LBG. This is due to LAEs being more shot noise dominated than LBGs at the luminosity limits of Stage 4.5. This increases the importance of lensing as well. As discussed in §4, the primary contributions to constraint improvement come from degeneracy breaking. This is visualized in Figure 11, which shows the marginalized contours of the full-shape approach at the $z = 3$ bin of Stage 4.5. In particular, the correlation coefficient between cosmological parameters Ω_m and h , and linear biases b are significantly reduced from ~ 0.5 to $\lesssim 0.05$ by the addition of galaxy-lensing cross-spectra. This indicates that the cross-spectra has broken degeneracy between linear bias and cosmology, as we have predicted. Note that degeneracy breaking does not necessarily reduce correlation coefficients and thus this only highlights some of the most noticeable degeneracy breakings. When RT is present, multi-tracer benefits from LAEs diminishes significantly with the constraints weakening by approximately 5%. This turns to an improvement when lensing is included ($\kappa \times \text{LBG} \rightarrow \kappa \times \text{LAE} \times \text{LBG}$), but the improvements remain less than 5%.

Figure 12 shows the Stage V constraints for all 3 scenarios, with both galaxy tracers included without RT. While there are sizable differences between scenarios, they are not drastic, especially with the inclusion of lensing. This indicates that σ_8 constraints are robust

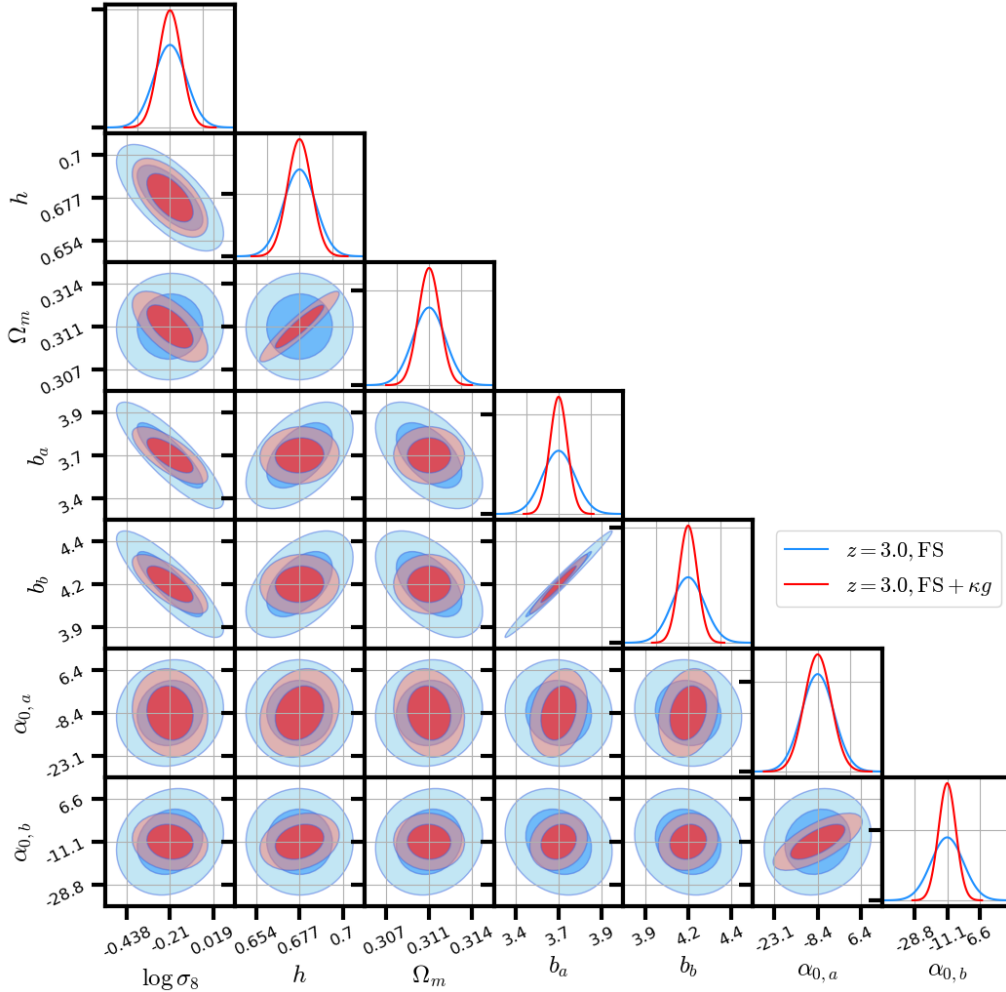


Figure 11: The marginalized contours of the full-shape approach to constraining growth. The contours shown are from the $z = 3$ bin of Stage 4.5, with and without galaxy-lensing cross-spectra. The contours show clear signs of degeneracy breaking from the addition of lensing. In particular, the correlation coefficient between cosmological parameters Ω_m and h , and linear biases b are significantly reduced from ~ 0.5 to $\lesssim 0.05$. Note that degeneracy breaking does not necessarily reduce of correlation coefficients.

to experiment designs.

6.2 Standard model

Multi-tracers will further assist next-generation LSS experiments to provide constraints similar to CMB experiments alone. Figure 13 shows a summary of forecasts. It does not include ω_b as it shows no influence from either multi-tracers nor RT, likely due to the prior dominat-

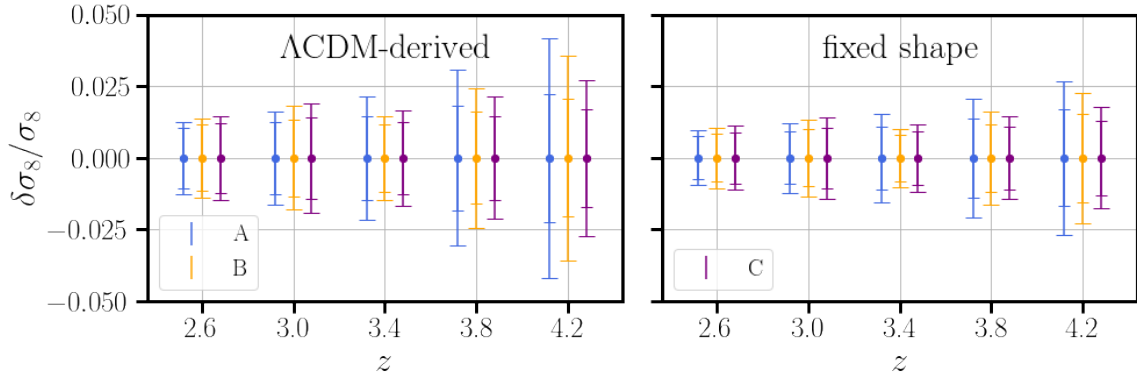


Figure 12: Relative constraints on $\sigma_8(z)$ from Stage V surveys in the Λ CDM-derived (left) and fixed shape (right) methods, with both LAEs and LBGs, without RT. The smaller cap sizes correspond to the constraints including CMB lensing. ‘A’, ‘B’, and ‘C’ each correspond to Plans A, B, and C of Stage V (Table 2). All error bars assume inclusion of all multi-tracer spectra.

ing the constraining power. Forecasts indicate that with a BBN prior, multi-tracers through LAEs will improve the constraints on all other cosmological parameters by $\lesssim 10\%$. Inclusion of lensing generally yields larger improvements, with the improvement varying from $\sim 20\%$ for h to $\sim 85\%$ for Ω_k . Overall, the improvements amount to $25 - 45\%$, with the exception of Ω_k at 89% .

With Planck primary priors, there are varying multi-tracer effects. Multi-tracers with LAEs on a LBG-only sample will have even less improvement compared to when using BBN priors, at $\sim 5\%$, but when lensing is included (i.e. $\text{LBG} \times \kappa \rightarrow \text{LAE} \times \text{LBG} \times \kappa$) the improvements increase, marking $\sim 35\%$ for h and ω_c . Similarly, the improvements from adding lensing vary across parameters, marking a wide range between $\sim 20\%$ to $\sim 65\%$. h and ω_c are again most affected, with constraints improving $\sim 60\%$ when adding lensing to the $\text{LAE} \times \text{LBG}$ sample. Refer to Figure 9 for specific parameter constraint improvements.

Inclusion of RT generally has little effect on the cosmological constraints, except for $\log(A_s)$ that experience significant effects for forecasts without κ due to reasons similar to σ_8 . The final constraints with inclusion of all tracers experience sub-percent effect from RT, however. Our results also indicate that Stage V designs provide constraints significantly stronger than that of Stage 4.5, regardless of the luminosity limits adopted.

6.3 Distances

One of the most important constraints from LSS surveys are the distance measurements made through the BAO peaks in the power-spectra. Previous work have forecasted that near-term surveys such as DESI, Euclid and HIRAX can measure angular diameter distance and Hubble parameter to sub-percent and percent precision, respectively, up to $z \sim 2$, and future experiments to sub-percent precision up to $z \sim 5$ [5]. We will follow the modelling methods used in ref. [5], marginalizing over linear bias and 15 polynomial coefficients defined as

$$P_{\text{obs}} = \alpha_{\parallel}^{-1} \alpha_{\perp}^{-2} P_{\text{recon}} + \sum_{n=0}^4 \sum_{m=0}^2 c_{nm} k^n \mu^{2m} \quad (6.1)$$

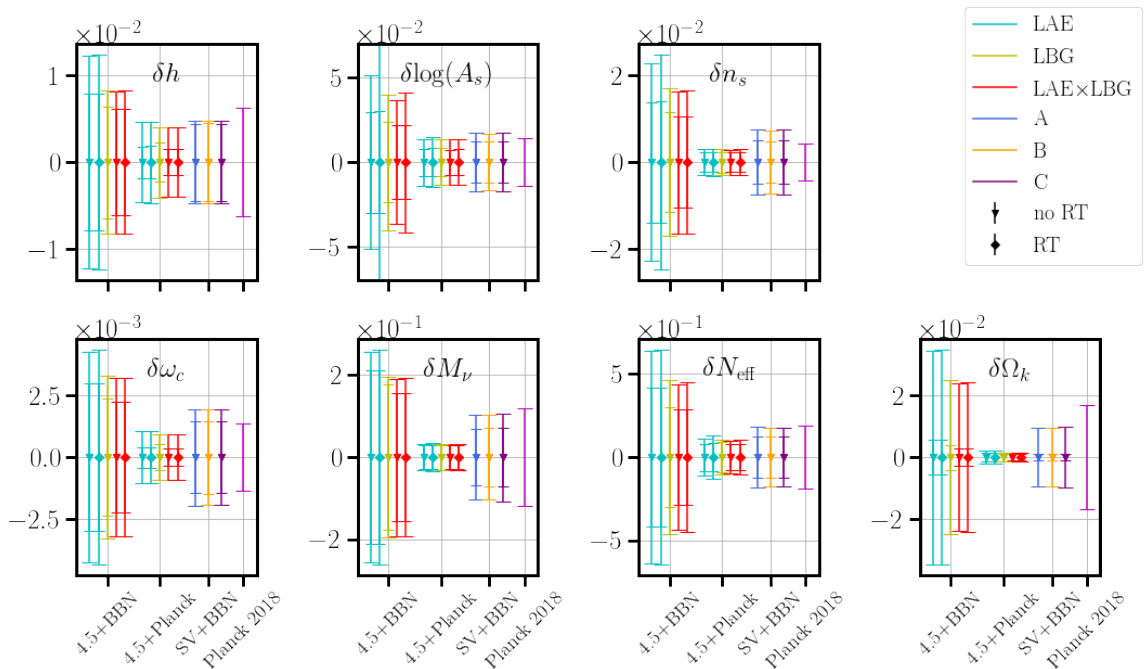


Figure 13: Λ CDM and extension results. The ‘4.5+BBN’, ‘4.5+Planck’ and ‘SV+BBN’ each refer to Stage 4.5 with a BBN prior, Stage 4.5 with a Planck prior, and Stage V with a BBN prior, respectively. ‘A’, ‘B’, and ‘C’ each correspond to Plans A, B, and C of Stage V (Table 2). The massive neutrino constraints include DESI BAO and lensing auto-spectra for all results. The magenta errorbars are the constraints given by Planck [69].

where α_{\parallel} and α_{\perp} are A-P parameters and P_{recon} is the post-reconstruction power-spectrum calculated within the Zeldovich approximation using the “RecSym” convention [70, 71]. We refer the reader to ref. [5] for further details about the model.

Our results, shown in Figure 14, show that Stage 4.5 will reach sub-percent precision in both distance measures in its entire redshift range $2.4 < z < 3.2$, with the aid of multi-tracers improving constraints by $\sim 10 - 15\%$. More significantly, these improvements are uninfluenced by the presence of RT. This is not surprising, given that BAOs are a well-localized feature with a known shape and the modelling process already marginalizes over any \mathbf{k} dependence for each spectrum beyond P_{recon} .

Forecasts for Stage V surveys, shown in Figure 15, indicate that future survey of such kind can improve and further extend these constraints up to $z = 4.4$. The comparable results between the different designs of Stage V indicate that such constraints are robust to the survey optimization, although fractional improvements can be gained at some redshifts in price for constraining power at other redshifts.

6.4 Neutrino mass and light relics

Variation of neutrino mass is a reasonable extension to the Λ CDM model. Measurements have yet to determine whether the neutrino mass hierarchy is normal ($m_{\nu_2} < m_{\nu_3}$, $\Sigma m_{\nu_i} \gtrsim 58\text{meV}$) or inverted ($m_{\nu_2} > m_{\nu_3}$, $\Sigma m_{\nu_i} \gtrsim 105\text{meV}$) [72]. Sum of neutrino masses can be constrained cosmologically by measuring its effect on power-spectra. As neutrinos transition

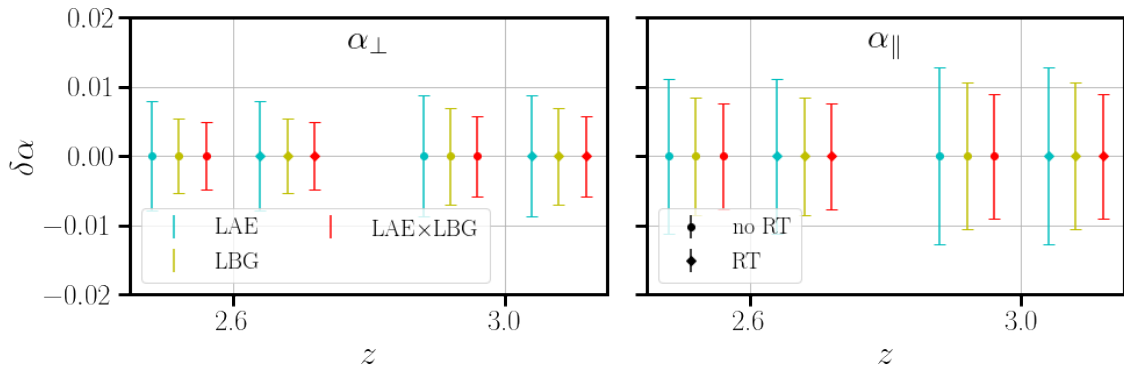


Figure 14: Stage 4.5 constraints on A-P parameters (α_{\perp} , α_{\parallel}), which can be interpreted as relative constraints on BAO parameters ($D_A(z)/r_d$, $r_d H(z)$), respectively. The inclusion of RT clearly have minimal effect for BAO constraints.

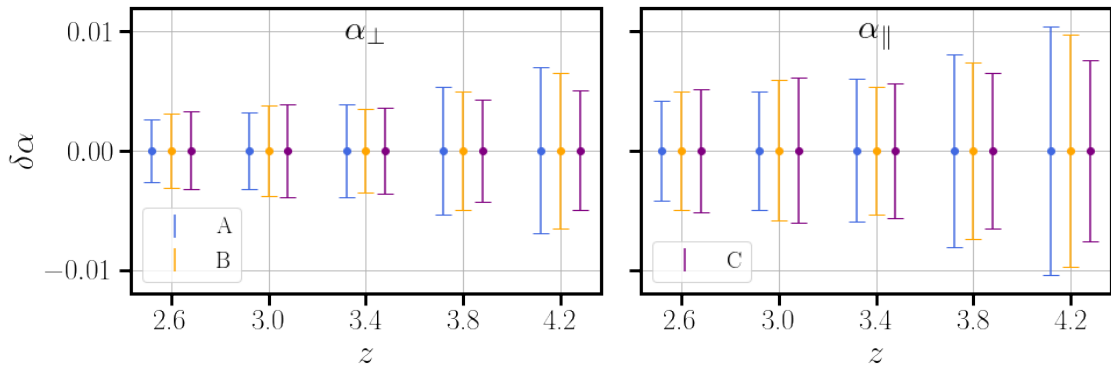


Figure 15: Stage V constraints for A-P parameters (α_{\perp} , α_{\parallel}), which can be interpreted as relative constraints on $D_A(z)/r_d$ and $r_d H(z)$, respectively. ‘A’, ‘B’, and ‘C’ each correspond to Plans A, B, and C of Stage V (Table 2). Each constraint assumes the inclusion of all multi-tracer spectra.

from relativistic to non-relativistic species at scale factor a_{nr} , neutrinos only cluster at large scales ($k \ll k_{\text{nr}} = a_{\text{nr}} H(a_{\text{nr}})$), and damp the power-spectra on smaller scales [5].

For neutrino mass ($M_{\nu} = \Sigma m_{\nu_i}$) forecasts, we include DESI BAO and SO lensing auto-spectrum for all results. The DESI BAO data included is from the Bright Galaxy Survey (BGS; [73, 74]), Luminous Red Galaxies (LRG; [74, 75]), and Emission Line Galaxies (ELG; [76]), post-reconstruction. We do not include the Lyman-alpha data due to its redshift overlap with next-generation facility galaxies. The results shown in Figure 13, show that Stage 4.5 will be able to constrain the total neutrino mass to 157meV (28meV) with BBN (Planck) priors. While improvements from individual tracers are $\lesssim 10\%$ for BBN priors and $\lesssim 4\%$ for Planck priors, the total improvement from both LAEs and lensing combined are double that, at 20% and 11% for BBN and Planck priors, respectively.

Ref. [5, 77–79] notes that improvement of τ measurements will significantly tighten M_{ν} measurements by removing the τ - A_s degeneracy in primary CMB. Ref. [80] has shown

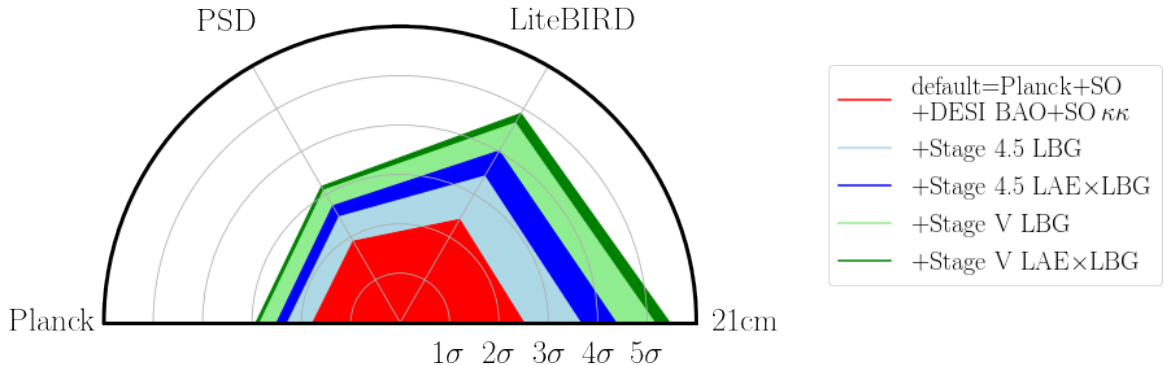


Figure 16: Fidelity of detection for normal neutrino mass hierarchy given τ constraints provided by external facilities. Each contour represents different information used for forecast. The red contour is only the default set of data, from Planck+SO CMB prior, DESI BAO measurements, and SO lensing auto-spectrum. The other contours include Stage 4.5 of Stage V galaxies and appropriate galaxy-lensing cross-correlations in addition to the default set. The labels show external constraints on τ that can be obtained currently or in the near-future. $\sigma(\tau)$ in each case are 0.0071 [5, 87, 88], 0.0058 [5, 79], 0.002 [83, 84], and 0.0009 [79], for Planck, Planck+SO+DESI (PSD), LiteBIRD, and 21cm surveys, respectively. In particular, the constraint provided by LiteBIRD is the cosmic variance limit [82] for CMB experiments.

that this leads to immense advantages when considering the τ -constraints provided by near-future CMB surveys. Multiple galaxy tracers allow us to further take advantage of this. Figure 16 shows the effect, by showing forecasts for σ 's towards normal hierarchy detection using external τ constraints from current and near-future sources. In particular, LiteBIRD [81] will be able to provide cosmic variance limited constraints on τ for CMB experiments at $\sigma(\tau) = 0.002$ [82–84]. At the tightest τ constraints from 21cm surveys [77, 79, 85, 86], the inclusion of LAEs will improve the measurements by 0.7σ and 0.3σ for Stage 4.5 and Stage V, respectively, allowing for the 5.5σ detection of the normal mass hierarchy.

The light relic forecasts on N_{eff} show that near future constraints from Stage 4.5 and Stage V will be comparable to or tighter than the Planck constraints. The assistance of multi-tracers are more significant with a BBN prior, with the total improvement at 38%. With a Planck prior, the help of both tracers decrease, marking a total improvement of 25%. Finally, we see that the choice of Stage V design has minimal effect on the final constraints, providing errors tighter than that of Planck using only galaxy tracers and a BBN prior.

6.5 Primordial features

Current constraints of inflation, primarily by CMB observations, are consistent with a simple, single scalar field slow-roll inflation. The (near) flatness of the inflationary potential leads

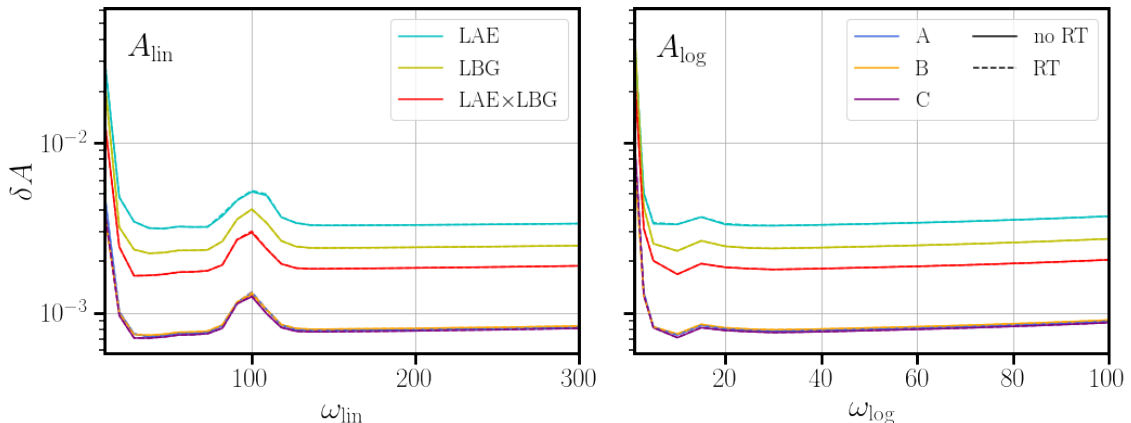


Figure 17: Forecast results for A_{lin} and A_{log} for a BBN-prior. ‘A’, ‘B’, and ‘C’ each correspond to Plans A, B, and C of Stage V (Table 2). The loss in δA_{lin} near $\omega_{\text{lin}} = 100$ with the BBN prior is due to the degeneracy with BAO [5], but this degeneracy is removed when using a Planck prior.

to a simple explanation of the nearly scale-invariant primordial power-spectrum. When formulating a model from a more fundamental basis, however, one often finds deviation from said scale-invariance [5, 89, 90]. A canonical subclass of such models approximate deviation from scale-invariance over a narrow range of scales, using oscillations in k or $\log k$. For this work, we model this as oscillations in the linear power-spectrum

$$P_m(k) \rightarrow [1 + A_{\text{lin}} \sin(\omega_{\text{lin}} k + \phi_{\text{lin}}) + A_{\text{log}} \sin(\omega_{\text{log}} \log k/k_* + \phi_{\text{log}})] P_m(k) \quad (6.2)$$

where $k_* = 0.05 h^{-1} \text{Mpc}$ is the pivot scale [5, 90, 91]. We fix ϕ_{lin} and ϕ_{log} to $\pi/2$ for all forecasts and characterize the change in constraining power as we vary ω_{lin} and ω_{log} .

Our results, shown in Figures 17 indicate that use of multiple galaxy tracers benefits our sensitivity by 8% for A_{lin} and 16% for A_{log} with BBN priors, and less than 2% for both with Planck priors. Furthermore, the inclusion of RT minimally affect the constraints, as increasing uncertainty in μ dependence does not directly alter our ability to detect k dependence. We find that these constraints are robust against crude optimization strategies for Stage V.

6.6 Early dark energy

While current measurements of cosmology are consistent with that of the cosmological constant Λ as the source of dark energy, dynamical dark energy is an active area of research. Early dark energy (EDE) is among these models, with Ω_{DE} rapidly dropping at high redshift. The specific model that we probe has the potential $V(\phi) \propto [1 - \cos(\phi/f)]^3$, where ϕ is a light scalar field [5, 92]. The field is parameterized by redshift z_c , where $f_{\text{EDE}} \equiv \rho_{\text{EDE}}/\rho_{\text{tot}}$ is maximum, and the initial value of the field $\theta_i \equiv \phi_i/f$. This model, as well as other major EDE models, invokes a phase shift in BAO when $z_c \gtrsim z_*$, where $z_* \sim 1100$ is recombination. Otherwise, when $z_c \lesssim z_*$, EDE damps the power-spectrum equally across scales for $k \gtrsim 0.01 h \text{Mpc}^{-1}$ [5]. This can be understood by simply considering the derivation for sound

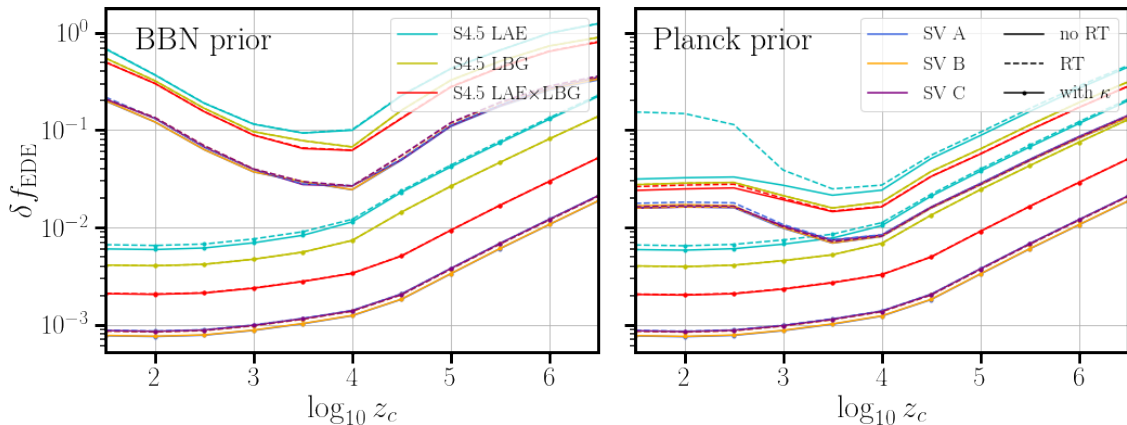


Figure 18: Forecast results for early dark energy. ‘S4.5’ refers to Stage-4.5, whereas ‘SV A’, ‘SV B’, and ‘SV C’ each correspond to Plans A, B, and C of Stage V (Table 2). RT induces a loss of constraining power at with a Planck prior due to the additional amplitude degeneracy.

horizon r_s and angular diameter distance $D_A(z)$

$$r_s = \int_{z_*}^{\infty} \frac{c_s(z)}{H(z)} dz \quad D_A(z) = \int_0^z \frac{dz}{H(z)} \quad (6.3)$$

When $z_c \gtrsim z_*$, the BAO scale is impacted by influence on r_s , while for $z_c \lesssim z_*$, there is no influence on either parameters (as long as $z < z_c$, which is always the case for realistic models and any quasi-near-time surveys). The phase shifts on BAO, or more specifically modifications of the Hubble parameter measurements from the CMB, has the potential to relieve the Hubble tension. For the forecasts in this section, we fix $\theta_i = 2.83$ and probe $1.5 < \log_{10}(z_c) < 6.5$ using CLASS_EDE [93].

The results shown in Figure 18 indicate that multi-tracers play a significant role in EDE constraints. While the improvements through LAEs alone remain modest at $\lesssim 10\%$ for both priors, lensing improves the constraints by 91% with a BBN prior and $\sim 64\%$ with a Planck prior, totalling together to 97% and 85%, respectively.

We also observe that composite constraint is affected marginally by the presence of RT, while for LAE-only constraints this is not always true. Ref. [5] makes note that LSS-only constraints (without RT) are worsened at low z_c ($z_c \lesssim z_*$) and attribute this to the degeneracy between the damping of power-spectra at $k \gtrsim 0.01 h \text{Mpc}^{-1}$, A_s and b . We recognize that for LAE-only constraints in the Planck prior case, RT significantly diminishes our constraining power further at this regime. This is entirely expected, as the variational f at linear-theory level introduces an additional degree of freedom on the existing amplitude degeneracy. Notably, the inclusion of lensing nearly recovers our constraining power lost from RT. This again suggests that the inclusion of lensing aids the breaking of degeneracy introduced by RT.

7 Conclusions

Next generation experiments in large-scale structure aim to probe the high redshift universe to constrain the Λ CDM model and its extensions. Modelling of large-scale structure using perturbation theory introduces nuisance parameters (Table 3) such as bias b_X , counter-terms α_{2n} , and stochastic terms N_{2n} in order to make predictions in a controlled manner. A major limitation to cosmological constraints are the degeneracy that these parameters introduce in the data, as well as inherent degeneracies between cosmological parameters. Tracing multiple different tracers at the same redshift, called the “multi-tracer” technique, may allow us to break these degeneracies by using the different dependence of tracers to each parameter. Next generation facilities may choose to do this with Lyman alpha emitters (LAEs), Lyman break galaxies (LBGs), and CMB lensing κ . With different large-scale biases (Figures 1, 2, or the lack thereof), these tracers will be well-suited for multi-tracer cosmology. In this work, we have compared forecasted cosmological constraints from single tracers, an “incomplete” multi-tracer technique (where one uses multiple galaxy tracers but only includes the two galaxy auto-spectra as signals neglecting the galaxy-galaxy cross-spectrum) and one which includes all available spectra.

We start with a generic investigation of the mechanism of multi-tracer cosmology, using σ_8 forecasts for a set of simplified tracers. We find that degeneracy breaking indeed drives a majority of the improvement in constraining power, in agreement with recent studies [64, 65].

We then apply the multi-tracer technique for Fisher forecasts of next generation surveys, namely “Stage 4.5”, inspired by DESI II, and “Stage V”, using both BBN and Planck primary priors. We find that the multi-tracer technique has varying effect on constraining power, as shown in Figure 9. In general, multi-tracer with LAEs on a LBG-only sample do not improve the constraints drastically with the improvements $\lesssim 15\%$ for most parameters. Interestingly, when using LAEs as an addition onto a $\kappa \times$ LBG sample, there are parameters that improve considerably, namely h and ω_c with a Planck prior, at $\sim 35\%$, and f_{EDE} at $\sim 60\%$. CMB lensing proves to be a better contribution to multi-tracers than LAEs in many cases, although the improvements cannot be compared on equal footing as they are adopted without any cost, while observing LAEs cost observation time that can otherwise be used for LBGs. With lensing, many of cosmological parameters being improved $\gtrsim 20\%$, with a factor of $\gtrsim 10$ improvement for f_{EDE} being the most drastic. Importantly, we find that these improvements aggregate well in general (e.g., for $\delta\sigma_8$ the $\sim 10\%$ and $\sim 20\%$ improvements from LAEs and lensing, respectively, lead to $\sim 30\%$ improvements when combined), proving that we are not in a regime where there are enough tracers that additional tracers become insignificant.

Where they overlap our results agree well with the recent study of ref. [65], although the results are presented differently. Ref. [65] quotes $\sim 50\%$ improvement in constraining power from multi-tracers with two galaxy samples, using $\sigma_{ST}/\sigma_{MT} - 1$ as their metric. We use $1 - \sigma_{MT}/\sigma_{ST}$ which leads to smaller quoted improvements, e.g. a 50% improvement in ref. [65] corresponds to a 33% improvement in our metric, bridging a significant portion of the apparent gap between the final results. Remaining differences in results can be attributed to differences in the galaxy samples used, such as the difference between galaxy biases. A similar comment can be made for differences between this work and ref. [94], which show improvements ranging from 5% to 33% from ELGs and LRGs. In both studies, there is a factor ~ 2 difference between linear biases, whereas LAE and LBG biases differ only by 30% at most (for Stage 4.5) in this work.

We also perform a crude optimization of Stage V survey designs by changing luminosity

limits for both LAEs and LBGs while keeping the total integration time fixed. We find that most Stage V constraints are robust to this optimization, leaving room for future optimization involving specific targets and observation techniques. A detailed study of survey optimization, including galaxy mix as a function of redshift, time-to-redshift and redshift efficiency factors, is left for future work.

A possible source of concern for the use of LAEs as cosmological probes is the impact of radiative transfer (RT), specifically the absorption and scattering of Ly α emission lines by neutral hydrogen near the LAE. By assuming that RT effects are small, we attempt a preliminary investigation of the impact of RT by including its effects at the linear theory level, ignoring higher order contributions. Forecasts using this model show that σ_8 loses nearly half of its multi-tracer gains by LAEs, and LAE-only forecasts experience significant loss of constraining power for σ_8 , A_s , neutrino mass, and early dark energy with Planck priors at low z_c due to the additional amplitude degeneracy. On the contrary, however, we find that other forecasts are fairly unaffected, and all constraints experience little effect for the final, three-tracer forecast. Of course, this treatment of RT is merely preliminary and a more complete calculation will be attempted in the future.

Acknowledgments

We thank Shi-Fan Chen for discussion on counterterm treatment, and Arjun Dey, Simone Ferraro, Noah Sailer, and Ruiyang Zhao for useful discussions throughout the course of this work. H.E. and M.W. are supported by the DOE. This research has made use of NASA's Astrophysics Data System and the arXiv preprint server. This research is supported by the Director, Office of Science, Office of High Energy Physics of the U.S. Department of Energy under Contract No. DE-AC02-05CH11231, and by the National Energy Research Scientific Computing Center, a DOE Office of Science User Facility under the same contract.

A Variance of measurements with correlation

In this section we walk through the calculation of the composite variance from two correlated measurements, leading to Eq. 4.5. Suppose that two measurements (x_1, x_2) are made drawing from a Gaussian distribution of mean μ and covariance C . The covariance matrix will be of the form

$$C = \begin{pmatrix} \sigma_1^2 & r\sigma_1\sigma_2 \\ r\sigma_1\sigma_2 & \sigma_2^2 \end{pmatrix} \quad (\text{A.1})$$

where $r \in [-1, 1]$ is the correlation coefficient. The probability of measuring (x_1, x_2) , then, is

$$P(x_1, x_2) \propto \exp\{(\vec{x} - \vec{\mu})^T C^{-1} (\vec{x} - \vec{\mu})/2\} \quad (\text{A.2})$$

where $\vec{x} = (x_1, x_2)$ and $\vec{\mu} = (\mu, \mu)$. Maximizing the likelihood of observation provides the best estimate of μ , with variance σ^2

$$\mu = \frac{\vec{1}^T C^{-1} \vec{x}}{\vec{1}^T C^{-1} \vec{1}}, \quad \sigma^2 = \frac{(1 - r^2)\sigma_1^2\sigma_2^2}{\sigma_1^2 - 2r\sigma_1\sigma_2 + \sigma_2^2} \quad (\text{A.3})$$

where $\vec{1} = (1, 1)$. Taking some limits with these expressions reveal important insights. In the fully uncorrelated case $r = 0$, one recovers the standard weighted average $\mu = (x_1/\sigma_1^2 + x_2/\sigma_2^2)(1/\sigma_1^2 + 1/\sigma_2^2)^{-1}$, $\sigma^2 = (1/\sigma_1^2 + 1/\sigma_2^2)^{-1}$. When two measurements are redundant, with

$\sigma_1 = \sigma_2$ and $r \rightarrow 1$, one obtains $\sigma^2 = \sigma_1^2$, as expected. The best case is where there is near full correlation $|r| \rightarrow 1$, with non-redundant information $\sigma_1 \neq \sigma_2$. Then, one obtains $\sigma^2 \rightarrow 0$.

B Conventions of limiting luminosity in literature

Literature from the astronomy community often use two different conventions to make note of their luminosity function integration range. In this section we show the conversion between the two conventions.

The first approach is to simply use the lower limit of the integral, e.g.

$$\bar{n} = \int_{L_{\text{lim}}}^{\infty} \Phi(L') dL' \quad (\text{B.1})$$

Another is to use the median, e.g. L_{med} , such that

$$\int_{L_{\text{med}}}^{\infty} \Phi(L') dL' = \frac{1}{2} \int_{L_{\text{lim}}}^{\infty} \Phi(L') dL' \quad (\text{B.2})$$

Note that in some authors place an explicit, finite upper limit on the integrals depending on the context. These definitions are extended for limiting line fluxes or magnitudes analogously. It is clear that with the luminosity function (LF) parameters, one can convert one to the other easily. For the regimes of our interest, the differences are typically $\sim 0.1 - 0.2$ in log-space.

C Counterterms

The theory of Lagrangian EFT has been developed in refs. [53, 95–110]. However in those works the cross-spectra between different tracers was not highlighted. In this appendix we briefly recap the key points of Lagrangian EFT, with a focus on the counterterms for the cross-spectra which have not appeared explicitly before. This will also allow us to make contact with the Eulerian approach of ref. [65], which has the same counterterm structure.

We will perform calculations at both the density field-level and the power-spectrum-level. The latter is a more precise follow-through of the calculation, as the expectation values are taken explicitly, but we will see that the former will yield the same result with a simpler interpretation.

We will start with the field-level interpretation. In Lagrangian EFT, the density field of a tracer is given by

$$\delta_a + (2\pi)^3 \delta_D(\mathbf{k}) = \int_{\mathbf{q}} F[\delta(q)] e^{i\mathbf{k} \cdot (\mathbf{q} + \Psi(\mathbf{q}))} \quad (\text{C.1})$$

where Ψ is the displacement field and the functional F describes the tracer's dependence on underlying fields using bias. For this section, we limit ourselves to linear order, $F = 1 + b_1 \delta$, with b_1 the Lagrangian bias. Including higher-order terms (δ^2 , s^2 , etc.) will not add to this section as their contributions to the counterterm will exceed one-loop order. For similar reasons we will limit ourselves to the linear solution of Ψ .

To obtain the counterterms, we begin by dividing the displacements into long-wavelength components and a short-wavelength component. The former are treated perturbatively, while the latter can only be constrained by symmetry arguments and are included as a derivative

expansion. Some of these terms correlate with the long-wavelength contributions while some do not. We refer to the former as counterterms and the latter as stochastic terms. These terms allow for the final results to be independent of the cutoff scale Λ used in defining the perturbative terms.

To linear order the (long-wavelength) displacement field Ψ^L is simply $(i\vec{k}/k^2)\delta_{\text{lin}}(k)$ [95]. In redshift space we apply an additional displacement along the line of sight [111]. Since $\dot{\Psi}^L = f\Psi^L$, in Hubble units, for the linear displacement the transition to redshift space is accomplished by multiplying the line-of-sight component of Ψ^L by $1 + f$. Then, in the absence of counterterms (i.e. absence of small-scale contributions), we obtain the Kaiser power spectrum by expanding the exponent $e^{i\mathbf{k}\cdot\Psi}$ as

$$e^{i\mathbf{k}\cdot\Psi(s)} \simeq 1 + i\mathbf{k}\cdot\Psi(s) = 1 + i\mathbf{k}\cdot[\Psi(q) + f\hat{n}(\hat{n}\cdot\Psi(q))] \quad (\text{C.2})$$

where q and s are the real-space and redshift-space coordinates, respectively. Substituting this to Eq. C.1 and using $\mathbf{k}\cdot\hat{n} = k\mu$ yields $\delta_a = ([1 + b_1^{(a)}] + f\mu^2)\delta_{\text{lin}}$, where $1 + b_1$ is equivalent to linear bias in Eulerian PT.

Now let us divide our displacement field into $\Psi = \Psi^L + c_0(t)\nabla\delta_{\text{lin}} + \epsilon_i + \dots$. The term $c_0\nabla\delta_{\text{lin}}$ is the first-order counterterm (i.e. due to small scale dynamics) contribution to Ψ allowed by symmetry, whereas ϵ is the stochastic noise. As the time-dependence of c_0 and ϵ are unknown, we gain additional degrees of freedom for $\dot{\Psi}$. Let us define this as c_2 and $\dot{\epsilon}$ such that

$$\Psi_i = \Psi_i^L + c_0\nabla\delta_{\text{lin}} + \epsilon_i \quad (\text{C.3})$$

$$\dot{\Psi}_i = \dot{\Psi}_i^L + c_2\nabla\delta_{\text{lin}} + \dot{\epsilon}_i \quad (\text{C.4})$$

Performing a direct expansion for small-scale contributions as we did for linear theory calculations, we find

$$\delta_a \supset \int_{\mathbf{q}} e^{i\mathbf{k}\cdot\mathbf{q}} \sum_n \frac{1}{n!} [ik_i(\Psi_i + \dot{\Psi}_{\hat{n},i})]^n \quad (\text{C.5})$$

$$\supset \int_{\mathbf{q}} e^{i\mathbf{k}\cdot\mathbf{q}} \left(-c_{a,0} - c_{a,2}\mu^2 + \frac{1}{2}(1 + f\mu^2)((\hat{k}_i\epsilon_i)^2 + (\hat{n}_i\dot{\epsilon}_i)^2\mu^2) \right) k^2\delta_{\text{lin}} \quad (\text{C.6})$$

where we use $\dot{\Psi}_{\hat{n},i}^L = \hat{n}_i\hat{n}_j\dot{\Psi}_j^L$ for shorthand and the subscripts a on coefficients allow for tracer-dependent small-scale dynamics (whereas stochastic contributions ϵ do not have tracer-dependence). Note that we have neglected terms that go as even powers of δ_{lin} or odd powers of $\epsilon, \dot{\epsilon}$ as they vanish when taking expectation values at the power-spectrum level.

To lowest order the counterterms for the autospectrum of tracer a are thus $k^2 P_{\text{lin}}$ times

$$2 \left([1 + b_1^{(a)}] + f\mu^2 \right) (-\tilde{c}_{a,0} + -\tilde{c}_{a,2}\mu^2 - \tilde{c}_4\mu^4) \quad (\text{C.7})$$

while those for the cross-spectrum between tracers a and b are $k^2 P_{\text{lin}}$ times

$$\left([1 + b_1^{(a)}] + f\mu^2 \right) (-\tilde{c}_{b,0} + -\tilde{c}_{b,2}\mu^2 - \tilde{c}_4\mu^4) + \left([1 + b_1^{(b)}] + f\mu^2 \right) (-\tilde{c}_{a,0} + -\tilde{c}_{a,2}\mu^2 - \tilde{c}_4\mu^4) \quad (\text{C.8})$$

where we have redefined coefficients for simplicity. The cross-spectra thus introduce no new free parameters beyond those already needed for the counterterms of the auto-spectra, and this increases the utility of the cross-spectrum in breaking degeneracies. Note that although \tilde{c}_4

is a shared contribution across tracers, in this work we will allow them to be tracer-dependent, in order to be conservative. We expect that this will change the results minimally.

Now, we will perform the calculation at the power-spectrum-level to see that our results above are indeed correct. To do this, we will follow the moment expansion approach [110, 112, 113]. In this approach, one uses the fact that the redshift space power-spectrum is a specific case of the moment generating function and expands it such that

$$\frac{k^3}{2\pi^2}P_s(\mathbf{k}) = \tilde{M}(\mathbf{J} = \mathbf{k}, \mathbf{k}) = \frac{k^3}{2\pi^2} \int d^3r e^{i\mathbf{k}\cdot\mathbf{r}} \left\langle (1 + \delta_g(\mathbf{x}_1))(1 + \delta_g(\mathbf{x}_2))e^{i\mathbf{k}\cdot\Delta\mathbf{u}} \right\rangle_{\mathbf{x}_1 - \mathbf{x}_2 = \mathbf{r}} \quad (\text{C.9})$$

$$= \frac{k^3}{2\pi^2} \sum_{n=0}^{\infty} \frac{i^n}{n!} k_{i_1} \dots k_{i_n} \tilde{\Xi}_{i_1 \dots i_n}^{(n)}(\mathbf{k}) \quad (\text{C.10})$$

where $\mathbf{u} = \hat{n}(\hat{n}\cdot\mathbf{v})/\mathcal{H}$ is the LOS velocity, $\Delta\mathbf{u} = \mathbf{u}(\mathbf{x}_1) - \mathbf{u}(\mathbf{x}_2)$ their difference, and $\tilde{\Xi}^{(n)}$ are Fourier transforms of the velocity moments

$$\tilde{\Xi}_{i_1 \dots i_n}^{(n)} = \langle (1 + \delta_1)(1 + \delta_2)\Delta\mathbf{u}_{i_1} \dots \Delta\mathbf{u}_{i_n} \rangle \quad . \quad (\text{C.11})$$

Notice that here, the first moment is simply the real-space power-spectrum and the higher moment contributions provide information about redshift space distortions (RSD). As RSD depend only on the line-of-sight component of velocities, the only non-vanishing contributions to P_s come from the LOS component of $\tilde{\Xi}$. With this in mind, we rewrite the equation above as

$$P_s(\mathbf{k}) = \sum_{n=0}^{\infty} \frac{i^n}{n!} (k\mu)^n \sum_{\ell=0}^n \tilde{\Xi}_{\ell}^{(n)} \mathcal{L}_{\ell}(\mu) \quad (\text{C.12})$$

where $\tilde{\Xi}_{\ell}^{(n)}$ are Legendre moments of the velocity moments.

Formally, counterterm contributions arise from UV-divergences that arise from contractions of operators at small distances. As our theory knows only of large-scale dynamics, the only constraints we have on these contributions are from symmetry. Those that appear in the final expression are

$$\langle \Psi_i \Psi_j \rangle \supset \beta_1 \delta_{ij} + \beta_2 \delta_{ij} \delta + \beta_3 \hat{k}_i \hat{k}_j \delta \quad (\text{C.13})$$

$$\langle \delta \Psi_i \rangle \supset \beta_4 i k_i \delta \quad (\text{C.14})$$

and similarly for contact terms with derivatives, e.g. $\Psi_i \dot{\Psi}_j \supset \dot{\beta}_1 \delta_{ij} + \dot{\beta}_2 \delta_{ij} \delta + \dot{\beta}_3 \hat{k}_i \hat{k}_j \delta$. Note that the coefficients β will depend on the fields in contact, e.g. $\Psi_i^a \Psi_j^b \supset \beta_1^{ab} \delta_{ij}$ and $\beta_1^{aa} \neq \beta_1^{ab}$. However, these will not yield new degrees of freedom for the cross-spectra since the underlying mechanism is tracer dependent, as described in Eq. C.3-C.4.

Using the above contributions, one can compute the contributions to each velocity

moment multipole. For example, we have

$$\ddot{W}_{ijk} = \langle \dot{\Delta}_i \dot{\Delta}_j \dot{\Delta}_k \rangle \quad (\text{C.15})$$

$$= \underbrace{\langle \dot{\Psi}_i(q_1) \dot{\Psi}_j(q_1) \dot{\Psi}_k(q_1) - (q_1 \rightarrow q_2) \rangle}_{\propto \langle \delta \rangle = 0 \text{ for c.t.}} + \langle \dot{\Psi}_{\{i}(q_1) \dot{\Psi}_j(q_2) \dot{\Psi}_k\}(q_2) - (q_1 \leftrightarrow q_2) \rangle \quad (\text{C.16})$$

$$\supset \left\langle \frac{2ik_{\{i}}{k^2} \delta_1 \left(\ddot{\beta}_1 \delta_{jk\}} + \ddot{\beta}_2 \delta_{jk\}} \delta_2 + \ddot{\beta}_3 \hat{k}_j \hat{k}_k \right) \delta_2 \right\rangle \quad (\text{C.17})$$

$$= \frac{2i}{k} P_L f \left(\ddot{\beta}_2 \hat{k}_{\{i} \delta_{jk\}} + 3 \ddot{\beta}_3 \hat{k}_i \hat{k}_j \hat{k}_k \right) \quad (\text{C.18})$$

Using the velocity moment expressions [49], we see that this contributes to the velocity moment multipoles

$$-i\tilde{\Xi}_{1,ct}^{(3)} = \frac{6}{k} P_L f \left(\ddot{\beta}_2 + \frac{3}{5} \ddot{\beta}_3 \right) \quad , \quad -i\tilde{\Xi}_{3,ct}^{(3)} = \frac{12}{5k} P_L f \ddot{\beta}_3 \quad (\text{C.19})$$

which in turn contributes

$$P_{s,ct} \supset k^2 P_L (\ddot{\beta}_2 f \mu^4 + \ddot{\beta}_3 f \mu^6) \quad (\text{C.20})$$

Note that for $n = 3$ we use the Legendre basis instead of the polynomial basis shown in the Appendix of [49]. Performing a similar computation for all terms, one obtains

$$P_s \supset k^2 P_L (\tilde{\beta}_1 + \beta_2 + \beta_3 - 2b\beta_4 - 2c_0 + (\dot{\tilde{\beta}}_1 + 2\dot{\beta}_2 + 2\dot{\beta}_3 - 2b\dot{\beta}_4 + \ddot{\beta}_2 - 2c_2) \mu^2 + (\ddot{\tilde{\beta}}_1 + \ddot{\beta}_3) \mu^4) (1 + b + f \mu^2) \quad (\text{C.21})$$

in agreement with the field-level calculation above, where β_1 's have been redefined for brevity³ and terms with c_0 and c_2 (as defined in Eq. C.3-C.4) come from non-contact counterterms.

References

- [1] J. A. Peacock, *Cosmological Physics*. Jan., 1999.
- [2] S. Dodelson, *Modern cosmology*. 2003.
- [3] S. Dodelson and F. Schmidt, *Modern Cosmology*. Elsevier Science, 2020.
- [4] D. Baumann, *Cosmology*. Cambridge University Press, 2022.
- [5] N. Sailer, E. Castorina, S. Ferraro, and M. White, *Cosmology at high redshift — a probe of fundamental physics*, *JCAP* **12** (2021), no. 12 049, [[arXiv:2106.09713](#)].
- [6] R. Ellis and K. Dawson, *SpecTel: A 10-12 meter class Spectroscopic Survey Telescope*, in *Bull. Am. Astron. Soc.*, vol. 51, p. 45, Sept., 2019. [[arXiv:1907.06797](#)].
- [7] K. Dawson, J. Frieman, K. Heitmann, et al., *Cosmic Visions Dark Energy: Small Projects Portfolio*, [[arXiv:1802.07216](#)].
- [8] A. Blanchard et al., *Gravitation And the Universe from large Scale-Structures: The GAUSS mission concept. Mapping the cosmic web up to the reionization era*, [[arXiv:2102.03931](#)].
- [9] D. J. Schlegel, S. Ferraro, G. Aldering, et al., *A Spectroscopic Road Map for Cosmic Frontier: DESI, DESI-II, Stage-5*, *arXiv e-prints* (Sept., 2022) [[arXiv:2209.03585](#)].

³Note that $\ddot{\tilde{\beta}}_1$ is determined by b , $\tilde{\beta}_1$, and $\dot{\tilde{\beta}}_1$, but this will not reduce the degrees of freedom due to degeneracy with $\ddot{\beta}_3$

- [10] S. Ferraro, N. Sailer, A. Slosar, and M. White, *Snowmass2021 Cosmic Frontier White Paper: Cosmology and Fundamental Physics from the three-dimensional Large Scale Structure*, *arXiv e-prints* (Mar., 2022) arXiv:2203.07506, [[arXiv:2203.07506](#)].
- [11] V. Desjacques, D. Jeong, and F. Schmidt, *Large-scale galaxy bias*, *Phys. Rep.* **733** (Feb., 2018) 1–193, [[arXiv:1611.09787](#)].
- [12] P. McDonald and U. Seljak, *How to evade the sample variance limit on measurements of redshift-space distortions*, *Journal of Cosmology and Astro-Particle Physics* **2009** (Oct., 2009) 007, [[arXiv:0810.0323](#)].
- [13] A. Lewis and A. Challinor, *Weak gravitational lensing of the CMB*, *Phys. Rep.* **429** (June, 2006) 1–65, [[astro-ph/0601594](#)].
- [14] D. Hanson, A. Challinor, and A. Lewis, *Weak lensing of the CMB*, *General Relativity and Gravitation* **42** (Sept., 2010) 2197–2218, [[arXiv:0911.0612](#)].
- [15] M. Giavalisco, *Lyman-Break Galaxies*, *Ann. Rev. Astron. & Astrophys.* **40** (2002) 579–641.
- [16] A. E. Shapley, *Physical Properties of Galaxies from $z = 2-4$* , *Ann. Rev. Astron. & Astrophys.* **49** (Sept., 2011) 525–580, [[arXiv:1107.5060](#)].
- [17] M. J. Wilson and M. White, *Cosmology with dropout selection: straw-man surveys & CMB lensing*, *Journal of Cosmology and Astro-Particle Physics* **2019** (Oct., 2019) 015, [[arXiv:1904.13378](#)].
- [18] M. Ouchi, Y. Ono, and T. Shibuya, *Observations of the Lyman- α Universe*, *Ann. Rev. Astron. & Astrophys.* **58** (Aug., 2020) 617–659, [[arXiv:2012.07960](#)].
- [19] M. Dijkstra, *Ly α emitting galaxies as a probe of reionisation*, *Publications of the Astronomical Society of Australia* **31** (2014) e040.
- [20] T. Garel, J. Blaizot, B. Guiderdoni, et al., *The UV, Lyman α , and dark matter halo properties of high-redshift galaxies*, *Mon. Not. R. Astron. Soc.* **450** (June, 2015) 1279–1294, [[arXiv:1503.06635](#)].
- [21] K.-S. Lee, E. Gawiser, C. Park, et al., *The one-hundred-deg² decam imaging in narrowbands (odin): Survey design and science goals*, 2023.
- [22] D. Sobral, S. Santos, J. Matthee, et al., *Slicing COSMOS with SC4k: the evolution of typical ly α emitters and the ly α escape fraction from $z \sim 2$ to 6*, *Monthly Notices of the Royal Astronomical Society* **476** (feb, 2018) 4725–4752.
- [23] A. A. Khostovan, D. Sobral, B. Mobasher, et al., *The clustering of typical ly α emitters from $z \sim 2.5-6$: host halo masses depend on ly α and UV luminosities*, *Monthly Notices of the Royal Astronomical Society* **489** (aug, 2019) 555–573.
- [24] A. Konno, M. Ouchi, K. Nakajima, et al., *Bright and faint ends of ly α luminosity functions at $z = 2$ determined by the subaru survey: Implications for agns, magnification bias, and ism h i evolution*, *The Astrophysical Journal* **823** (may, 2016) 20.
- [25] M. Ouchi, K. Shimasaku, M. Akiyama, et al., *The Subaru/XMM-Newton Deep Survey (SXDS). IV. Evolution of Ly α Emitters from $z = 3.1$ to 5.7 in the 1 deg² Field: Luminosity Functions and AGN*, *Astrophys. J. Suppl.* **176** (June, 2008) 301–330, [[arXiv:0707.3161](#)].
- [26] L. Guaita, E. Gawiser, N. Padilla, et al., *Ly α -emitting galaxies at $z = 2.1$ in ecdf-s: Building blocks of typical present-day galaxies?**, *The Astrophysical Journal* **714** (apr, 2010) 255.
- [27] R. Bielby, P. Tummuangpak, T. Shanks, et al., *The vlt lbg redshift survey - v. characterising the $z = 3.1$ lyman alpha emitter population*, *Monthly Notices of the Royal Astronomical Society* **456** (01, 2015).
- [28] Y. Shioya, Y. Taniguchi, S. S. Sasaki, et al., *Photometric properties of ly α emitters at $z \approx 4.86$ in the cosmos 2 square degree field**, *The Astrophysical Journal* **696** (apr, 2009) 546.

- [29] C.-N. Hao, J.-S. Huang, X. Xia, et al., *A deep Ly α survey in ecdf-s and cosmos. i. general properties of Ly α emitters at $z \sim 2$* , *The Astrophysical Journal* **864** (sep, 2018) 145.
- [30] E. Gawiser, H. Francke, K. Lai, et al., *Ly α -emitting galaxies at $z = 3.1$: L^* progenitors experiencing rapid star formation**, *The Astrophysical Journal* **671** (dec, 2007) 278.
- [31] M. Ouchi, K. Shimasaku, H. Furusawa, et al., *Statistics of 207 Ly α emitters at a redshift near 7: Constraints on reionization and galaxy formation models**, *The Astrophysical Journal* **723** (oct, 2010) 869.
- [32] P. Schechter, *An analytic expression for the luminosity function for galaxies.*, *Astrophys. J.* **203** (Jan., 1976) 297–306.
- [33] R. Takahashi, M. Sato, T. Nishimichi, et al., *Revising the Halofit Model for the Nonlinear Matter Power Spectrum*, *Astrophys. J.* **761** (Dec., 2012) 152, [[arXiv:1208.2701](https://arxiv.org/abs/1208.2701)].
- [34] D. Blas, J. Lesgourgues, and T. Tram, *The Cosmic Linear Anisotropy Solving System (CLASS). Part II: Approximation schemes*, *Journal of Cosmology and Astro-Particle Physics* **7** (July, 2011) 034, [[arXiv:1104.2933](https://arxiv.org/abs/1104.2933)].
- [35] M. Tegmark and P. J. E. Peebles, *The Time Evolution of Bias*, *Astrophys. J. Lett.* **500** (June, 1998) L79–L82, [[astro-ph/9804067](https://arxiv.org/abs/astro-ph/9804067)].
- [36] N. A. Reddy, C. C. Steidel, M. Pettini, et al., *Multiwavelength Constraints on the Cosmic Star Formation History from Spectroscopy: The Rest-Frame Ultraviolet, H α , and Infrared Luminosity Functions at Redshifts $1.9 < z < 3.4$* , *Astrophys. J. Suppl.* **175** (Mar., 2008) 48–85, [[arXiv:0706.4091](https://arxiv.org/abs/0706.4091)].
- [37] M. A. Malkan, D. P. Cohen, M. Maruyama, et al., *Lyman-break galaxies at $z \sim 3$ in the Subaru deep field: Luminosity function, clustering, and [o iii] emission*, *The Astrophysical Journal* **850** (nov, 2017) 5, [[arXiv:1711.04787](https://arxiv.org/abs/1711.04787)].
- [38] Y. Ono, M. Ouchi, Y. Harikane, et al., *Great optically luminous dropout research using Subaru HSC (GOLDRUSH). i. UV luminosity functions at $z \sim 4-7$ derived with the half-million dropouts on the 100 deg² sky†*, *Publications of the Astronomical Society of Japan* **70** (nov, 2017) [[arXiv:1704.06004](https://arxiv.org/abs/1704.06004)].
- [39] P. Madau, *Radiative Transfer in a Clumpy Universe: The Colors of High-Redshift Galaxies*, *Astrophys. J.* **441** (Mar., 1995) 18.
- [40] A. Dey and D. Schlegel, “Private communications.”
- [41] **LSST Dark Energy Science** Collaboration, D. Alonso et al., *The LSST Dark Energy Science Collaboration (DESC) Science Requirements Document*, [[arXiv:1809.01669](https://arxiv.org/abs/1809.01669)].
- [42] L. S. Collaboration, P. A. Abell, J. Allison, et al., *Lsst science book, version 2.0*, 2009.
- [43] N. Galitzki, A. Ali, K. S. Arnold, et al., *The Simons Observatory: instrument overview*, in *Millimeter, Submillimeter, and Far-Infrared Detectors and Instrumentation for Astronomy IX*, vol. 10708 of *Society of Photo-Optical Instrumentation Engineers (SPIE) Conference Series*, p. 1070804, July, 2018. [[arXiv:1808.04493](https://arxiv.org/abs/1808.04493)].
- [44] S.-F. Chen, Z. Vlah, E. Castorina, and M. White, *Redshift-Space Distortions in Lagrangian Perturbation Theory*, *arXiv e-prints* (Dec., 2020) arXiv:2012.04636, [[arXiv:2012.04636](https://arxiv.org/abs/2012.04636)].
- [45] M. White, R. Zhou, J. DeRose, et al., *Cosmological constraints from the tomographic cross-correlation of DESI Luminous Red Galaxies and Planck CMB lensing*, *Journal of Cosmology and Astro-Particle Physics* **2022** (Feb., 2022) 007, [[arXiv:2111.09898](https://arxiv.org/abs/2111.09898)].
- [46] S.-F. Chen, Z. Vlah, and M. White, *A new analysis of galaxy 2-point functions in the BOSS survey, including full-shape information and post-reconstruction BAO*, *Journal of Cosmology and Astro-Particle Physics* **2022** (Feb., 2022) 008, [[arXiv:2110.05530](https://arxiv.org/abs/2110.05530)].

- [47] S.-F. Chen, M. White, J. DeRose, and N. Kokron, *Cosmological analysis of three-dimensional BOSS galaxy clustering and Planck CMB lensing cross correlations via Lagrangian perturbation theory*, *Journal of Cosmology and Astro-Particle Physics* **2022** (July, 2022) 041, [[arXiv:2204.10392](#)].
- [48] M. Maus, S. Chen, M. White, et al., *An analysis of parameter compression and full-modeling techniques with Velocileptors for DESI 2024 and beyond*, *arXiv e-prints* (Apr., 2024) arXiv:2404.07312, [[arXiv:2404.07312](#)].
- [49] S.-F. Chen, Z. Vlah, and M. White, *Consistent Modeling of Velocity Statistics and Redshift-Space Distortions in One-Loop Perturbation Theory*, *JCAP* **07** (2020) 062, [[arXiv:2005.00523](#)].
- [50] S.-F. Chen, Z. Vlah, and M. White, *Modeling features in the redshift-space halo power spectrum with perturbation theory*, *arXiv e-prints* (July, 2020) arXiv:2007.00704, [[arXiv:2007.00704](#)].
- [51] R. K. Sheth and G. Tormen, *Large-scale bias and the peak background split*, *Mon. Not. R. Astron. Soc.* **308** (Sept., 1999) 119–126, [[astro-ph/9901122](#)].
- [52] S. Cole and N. Kaiser, *Biased clustering in the cold dark matter cosmogony*, *Mon. Not. R. Astron. Soc.* **237** (Apr., 1989) 1127–1146.
- [53] M. White, *The Zel’dovich approximation*, *Mon. Not. R. Astron. Soc.* **439** (Apr., 2014) 3630–3640, [[arXiv:1401.5466](#)].
- [54] M. M. Abidi and T. Baldauf, *Cubic halo bias in Eulerian and Lagrangian space*, *Journal of Cosmology and Astro-Particle Physics* **2018** (July, 2018) 029, [[arXiv:1802.07622](#)].
- [55] M. Loverde and N. Afshordi, *Extended Limber approximation*, *Phys. Rev. D* **78** (Dec., 2008) 123506, [[arXiv:0809.5112](#)].
- [56] B. R. Frieden, *Physics from Fisher Information: A Unification*. Cambridge University Press, 1998.
- [57] M. Tegmark, *Measuring cosmological parameters with galaxy surveys*, *Physical Review Letters* **79** (nov, 1997) 3806–3809.
- [58] M. S. Vogeley and A. S. Szalay, *Eigenmode Analysis of Galaxy Redshift Surveys. I. Theory and Methods*, *Astrophys. J.* **465** (July, 1996) 34, [[astro-ph/9601185](#)].
- [59] M. White, Y.-S. Song, and W. J. Percival, *Forecasting cosmological constraints from redshift surveys*, *Mon. Not. R. Astron. Soc.* **397** (Aug., 2009) 1348–1354, [[arXiv:0810.1518](#)].
- [60] S.-F. Chen, E. Castorina, M. White, and A. Slosar, *Synergies between radio, optical and microwave observations at high redshift*, *Journal of Cosmology and Astro-Particle Physics* **2019** (July, 2019) 023, [[arXiv:1810.00911](#)].
- [61] Euclid Collaboration, A. Blanchard, S. Camera, et al., *Euclid preparation. VII. Forecast validation for Euclid cosmological probes*, *Astron. Astrophys.* **642** (Oct., 2020) A191, [[arXiv:1910.09273](#)].
- [62] G. M. Bernstein and Y.-C. Cai, *Cosmology without cosmic variance*, *Mon. Not. R. Astron. Soc.* **416** (Oct., 2011) 3009–3016, [[arXiv:1104.3862](#)].
- [63] C. Blake, I. K. Baldry, J. Bland-Hawthorn, et al., *Galaxy And Mass Assembly (GAMA): improved cosmic growth measurements using multiple tracers of large-scale structure*, *Mon. Not. R. Astron. Soc.* **436** (Dec., 2013) 3089–3105, [[arXiv:1309.5556](#)].
- [64] T. Mergulhão, H. Rubira, R. Voivodic, and L. R. Abramo, *The effective field theory of large-scale structure and multi-tracer*, *Journal of Cosmology and Astroparticle Physics* **2022** (apr, 2022) 021.

- [65] T. Mergulhão, H. Rubira, and R. Voivodic, *The effective field theory of large-scale structure and multi-tracer ii: redshift space and realistic tracers*, 2023.
- [66] Z. Zheng, R. Cen, H. Trac, and J. Miralda-Escudé, *Radiative Transfer Modeling of Ly α Emitters. II. New Effects on Galaxy Clustering*, *Astrophys. J.* **726** (Jan., 2011) 38, [[arXiv:1003.4990](#)].
- [67] C. Behrens, C. Byrohl, S. Saito, and J. C. Niemeyer, *The impact of Lyman- α radiative transfer on large-scale clustering in the Illustris simulation*, *Astron. Astrophys.* **614** (June, 2018) A31, [[arXiv:1710.06171](#)].
- [68] R. Momose, K. Shimasaku, K. Nagamine, et al., *Catch Me if You Can: Biased Distribution of Ly α -emitting Galaxies according to the Viewing Direction*, *Astrophys. J. Lett.* **912** (May, 2021) L24, [[arXiv:2104.10580](#)].
- [69] Planck Collaboration, N. Aghanim, Y. Akrami, et al., *Planck 2018 results. VI. Cosmological parameters*, *arXiv e-prints* (July, 2018) arXiv:1807.06209, [[arXiv:1807.06209](#)].
- [70] M. White, *Reconstruction within the Zeldovich approximation*, *Mon. Not. R. Astron. Soc.* **450** (July, 2015) 3822–3828, [[arXiv:1504.03677](#)].
- [71] S.-F. Chen, Z. Vlah, and M. White, *The reconstructed power spectrum in the Zeldovich approximation*, *Journal of Cosmology and Astro-Particle Physics* **2019** (Sept., 2019) 017, [[arXiv:1907.00043](#)].
- [72] K. N. Abazajian, P. Adshead, Z. Ahmed, et al., *CMB-S4 Science Book, First Edition*, *ArXiv e-prints* (Oct., 2016) [[arXiv:1610.02743](#)].
- [73] C. Hahn, M. J. Wilson, O. Ruiz-Macias, et al., *The desi bright galaxy survey: Final target selection, design, and validation*, *The Astronomical Journal* **165** (May, 2023) 253.
- [74] DESI Collaboration, A. Aghamousa, J. Aguilar, et al., *The DESI Experiment Part I: Science, Targeting, and Survey Design*, *ArXiv e-prints* (Oct., 2016) [[arXiv:1611.00036](#)].
- [75] R. Zhou, S. Ferraro, M. White, et al., *Desi luminous red galaxy samples for cross-correlations*, *Journal of Cosmology and Astroparticle Physics* **2023** (Nov., 2023) 097.
- [76] N. Mostek, A. L. Coil, M. Cooper, et al., *The deep2 galaxy redshift survey: Clustering dependence on galaxy stellar mass and star formation rate at $z \sim 1$* , *The Astrophysical Journal* **767** (Mar., 2013) 89.
- [77] A. Liu, J. R. Pritchard, R. Allison, et al., *Eliminating the optical depth nuisance from the CMB with 21 cm cosmology*, *Phys. Rev. D* **93** (2016), no. 4 043013, [[arXiv:1509.08463](#)].
- [78] A. Chudaykin and M. M. Ivanov, *Measuring neutrino masses with large-scale structure: Euclid forecast with controlled theoretical error*, *Journal of Cosmology and Astro-Particle Physics* **2019** (Nov, 2019) 034, [[arXiv:1907.06666](#)].
- [79] N. Sailer, S.-F. Chen, and M. White, *Optical depth to reionization from perturbative 21 cm clustering*, *JCAP* **10** (2022) 007, [[arXiv:2205.11504](#)].
- [80] N. Sailer, S. Ferraro, and M. White, “Measuring neutrino masses from the cosmic frontier.”.
- [81] H. Sugai, P. A. R. Ade, Y. Akiba, et al., *Updated design of the cmb polarization experiment satellite litebird*, *Journal of Low Temperature Physics* **199** (Jan, 2020) 1107–1117.
- [82] D. J. Watts, B. Wang, A. Ali, et al., *A projected estimate of the reionization optical depth using the class experiment’s sample variance limited e-mode measurement*, *The Astrophysical Journal* **863** (Aug., 2018) 121.
- [83] E. Allys, K. Arnold, J. Aumont, et al., *Probing cosmic inflation with the litebird cosmic microwave background polarization survey*, *Progress of Theoretical and Experimental Physics* **2023** (Nov., 2022).

- [84] E. D. Valentino, T. Brinckmann, M. Gerbino, et al., *Exploring cosmic origins with core: Cosmological parameters*, *Journal of Cosmology and Astroparticle Physics* **2018** (Apr., 2018) 017–017.
- [85] W. Qin, K. Schutz, A. Smith, et al., *An Effective Bias Expansion for 21 cm Cosmology in Redshift Space*, [arXiv:2205.06270](#).
- [86] G. Shmueli, D. Sarkar, and E. D. Kovetz, *Mitigating the optical depth degeneracy in the cosmological measurement of neutrino masses using 21-cm observations*, 2023.
- [87] Planck Collaboration, Y. Akrami, F. Arroja, et al., *Planck 2018 results. I. Overview and the cosmological legacy of Planck*, *arXiv e-prints* (July, 2018) arXiv:1807.06205, [[arXiv:1807.06205](#)].
- [88] Pagano, L., Delouis, J.-M., Mottet, S., et al., *Reionization optical depth determination from planck hfi data with ten percent accuracy*, *A&A* **635** (2020) A99.
- [89] A. Slosar, R. Mandelbaum, and D. Eisenstein, *Dark Energy and Modified Gravity*, *Bull. Am. Astron. Soc.* **51** (May, 2019) 97, [[arXiv:1903.12016](#)].
- [90] F. Beutler, M. Biagetti, D. Green, et al., *Primordial features from linear to nonlinear scales*, *Physical Review Research* **1** (Dec., 2019) 033209, [[arXiv:1906.08758](#)].
- [91] M. Ballardini, F. Finelli, C. Fedeli, and L. Moscardini, *Probing primordial features with future galaxy surveys*, *JCAP* **10** (2016) 041, [[arXiv:1606.03747](#)]. [Erratum: JCAP 04, E01 (2018)].
- [92] V. Poulin, T. L. Smith, T. Karwal, and M. Kamionkowski, *Early dark energy can resolve the hubble tension*, *Physical Review Letters* **122** (Jun, 2019).
- [93] J. C. Hill, E. McDonough, M. W. Toomey, and S. Alexander, *Early Dark Energy Does Not Restore Cosmological Concordance*, *arXiv e-prints* (Mar., 2020) arXiv:2003.07355, [[arXiv:2003.07355](#)].
- [94] R. Zhao, X. Mu, R. Gsponer, et al., *A multi-tracer analysis for the eboss galaxy sample based on the effective field theory of large-scale structure*, 2023.
- [95] Y. B. Zel'dovich, *Gravitational instability: An approximate theory for large density perturbations.*, *Astron. Astrophys.* **5** (Mar., 1970) 84–89.
- [96] T. Buchert, *A class of solutions in Newtonian cosmology and the pancake theory*, *Astron. Astrophys.* **223** (Oct., 1989) 9–24.
- [97] F. Moutarde, J.-M. Alimi, F. R. Bouchet, et al., *Precollapse scale invariance in gravitational instability*, *Astrophys. J.* **382** (Dec., 1991) 377–381.
- [98] E. Hivon, F. R. Bouchet, S. Colombi, and R. Juszkiewicz, *Redshift distortions of clustering: a Lagrangian approach.*, *Astron. Astrophys.* **298** (June, 1995) 643, [[astro-ph/9407049](#)].
- [99] A. N. Taylor and A. J. S. Hamilton, *Non-linear cosmological power spectra in real and redshift space*, *Mon. Not. R. Astron. Soc.* **282** (Oct., 1996) 767–778, [[astro-ph/9604020](#)].
- [100] V. Zheligovsky and U. Frisch, *Time-analyticity of Lagrangian particle trajectories in ideal fluid flow*, *Journal of Fluid Mechanics* **749** (June, 2014) 404–430, [[arXiv:1312.6320](#)].
- [101] T. Matsubara, *Recursive solutions of Lagrangian perturbation theory*, *Phys. Rev. D* **92** (July, 2015) 023534, [[arXiv:1505.01481](#)].
- [102] M. McQuinn and M. White, *Cosmological perturbation theory in 1+1 dimensions*, *Journal of Cosmology and Astro-Particle Physics* **1** (Jan., 2016) 043, [[arXiv:1502.07389](#)].
- [103] Z. Vlah, E. Castorina, and M. White, *The Gaussian streaming model and convolution Lagrangian effective field theory*, *Journal of Cosmology and Astro-Particle Physics* **12** (Dec., 2016) 007, [[arXiv:1609.02908](#)].

- [104] T. Matsubara, *Resumming cosmological perturbations via the Lagrangian picture: One-loop results in real space and in redshift space*, *Phys. Rev. D* **77** (Mar., 2008) 063530, [[arXiv:0711.2521](#)].
- [105] T. Matsubara, *Nonlinear perturbation theory with halo bias and redshift-space distortions via the Lagrangian picture*, *Phys. Rev. D* **78** (Oct., 2008) 083519, [[arXiv:0807.1733](#)].
- [106] J. Carlson, B. Reid, and M. White, *Convolution Lagrangian perturbation theory for biased tracers*, *Mon. Not. R. Astron. Soc.* **429** (Feb., 2013) 1674–1685, [[arXiv:1209.0780](#)].
- [107] R. A. Porto, L. Senatore, and M. Zaldarriaga, *The Lagrangian-space Effective Field Theory of large scale structures*, *Journal of Cosmology and Astro-Particle Physics* **5** (May, 2014) 022, [[arXiv:1311.2168](#)].
- [108] Z. Vlah, M. White, and A. Aviles, *A Lagrangian effective field theory*, *Journal of Cosmology and Astro-Particle Physics* **9** (Sept., 2015) 014, [[arXiv:1506.05264](#)].
- [109] Z. Vlah, U. Seljak, M. Yat Chu, and Y. Feng, *Perturbation theory, effective field theory, and oscillations in the power spectrum*, *Journal of Cosmology and Astro-Particle Physics* **2016** (Mar, 2016) 057, [[arXiv:1509.02120](#)].
- [110] Z. Vlah and M. White, *Exploring redshift-space distortions in large-scale structure*, *Journal of Cosmology and Astro-Particle Physics* **2019** (Mar, 2019) 007, [[arXiv:1812.02775](#)].
- [111] N. Kaiser, *Clustering in real space and in redshift space*, *Mon. Not. R. Astron. Soc.* **227** (July, 1987) 1–21.
- [112] U. Seljak and P. McDonald, *Distribution function approach to redshift space distortions*, *Journal of Cosmology and Astro-Particle Physics* **11** (Nov., 2011) 039, [[arXiv:1109.1888](#)].
- [113] Z. Vlah, U. Seljak, T. Okumura, and V. Desjacques, *Distribution function approach to redshift space distortions. Part V: perturbation theory applied to dark matter halos*, *Journal of Cosmology and Astro-Particle Physics* **10** (Oct., 2013) 053, [[arXiv:1308.6294](#)].